

Indian Ocean Variability in the CMIP5 Multimodel Ensemble: The Basin Mode

YAN DU,* SHANG-PING XIE,⁺ YA-LI YANG,* XIAO-TONG ZHENG,[#] LIN LIU,[@] AND GANG HUANG[&]

** State Key Laboratory of Tropical Oceanography, South China Sea Institute of Oceanology,
Chinese Academy of Sciences, Guangzhou, China*

*⁺ International Pacific Research Center and Department of Meteorology, University of Hawai'i at Mānoa, Honolulu,
Hawaii, and Physical Oceanography Laboratory, Ocean University of China, Qingdao, China, and
Scripps Institution of Oceanography, University of California, San Diego, La Jolla, California*

*[#] Physical Oceanography Laboratory and Key Laboratory of Ocean–Atmosphere Interaction and
Climate in Universities of Shandong, Ocean University of China, Qingdao, China*

[@] First Institute of Oceanography, State Oceanic Administration, Qingdao, China

*[&] Key Laboratory of Regional Climate–Environment Research for Temperate East Asia, Institute of Atmospheric Physics,
Chinese Academy of Sciences, Beijing, China*

(Manuscript received 24 September 2012, in final form 14 March 2013)

ABSTRACT

This study evaluates the simulation of the Indian Ocean Basin (IOB) mode and relevant physical processes in models from phase 5 of the Coupled Model Intercomparison Project (CMIP5). Historical runs from 20 CMIP5 models are available for the analysis. They reproduce the IOB mode and its close relationship to El Niño–Southern Oscillation (ENSO). Half of the models capture key IOB processes: a downwelling oceanic Rossby wave in the southern tropical Indian Ocean (TIO) precedes the IOB development in boreal fall and triggers an antisymmetric wind anomaly pattern across the equator in the following spring. The anomalous wind pattern induces a second warming in the north Indian Ocean (NIO) through summer and sustains anticyclonic wind anomalies in the northwest Pacific by radiating a warm tropospheric Kelvin wave. The second warming in the NIO is indicative of ocean–atmosphere interaction in the interior TIO. More than half of the models display a double peak in NIO warming, as observed following El Niño, while the rest show only one winter peak. The intermodel diversity in the characteristics of the IOB mode seems related to the thermocline adjustment in the south TIO to ENSO-induced wind variations. Almost all the models show multidecadal variations in IOB variance, possibly modulated by ENSO.

1. Introduction

Interannual basin-wide sea surface temperature (SST) warming over the tropical Indian Ocean (TIO) is highly correlated with El Niño–Southern Oscillation (ENSO) (Klein et al. 1999; Saji et al. 2006). Recent diagnostic studies reveal that this Indian Ocean Basin (IOB) mode is not a passive response to ENSO but involves air–sea interaction in the TIO and exerts important climatic influences on climate over the northwest Pacific (NWP) (Yang et al. 2007; Xie et al. 2009, 2010; Du et al. 2009, 2011; Huang et al. 2010) and Australia (e.g., Taschetto et al. 2011).

In the empirical orthogonal function (EOF) analysis, the basin-wide warming/cooling is the first mode and reaches a maximum during March–May, about one season after the mature phase of ENSO. Early studies revealed surface heat fluxes, specifically, the wind-induced latent heat flux and cloud-induced shortwave radiation flux anomalies, are important for this warming (Klein et al. 1999; Alexander et al. 2002; Ohba and Ueda 2005). In response to El Niño, the atmospheric circulation and convection weaken over the TIO, resulting in the increase of solar radiation and decrease of latent heat flux loss. Both contribute to the SST warming.

Recent studies found that the SST warming in the Indian Ocean has regional features with distinct evolutions and mechanisms. In the southwest TIO (SWIO), both heat budget analysis and model investigations indicated that surface fluxes could not explain the warming and suggested the importance of ocean dynamics (Klein

Corresponding author address: Yan Du, State Key Laboratory of Tropical Oceanography, South China Sea Institute of Oceanology, 164 West Xingang Road, Guangzhou 510301, China.
E-mail: duyan@scsio.ac.cn

et al. 1999; Lau and Nath 2003). There, the positive curls between the weak equatorial westerlies and the easterly trades to the south maintain upwelling and, thus, a thermocline dome in the climatology (Hermes and Reason 2008; Yokoi et al. 2008), conducive to subsurface influence on SST variability. During an El Niño event, an anticyclonic atmospheric circulation over the southeast TIO (SEIO) forces a downwelling Rossby wave. This downwelling Rossby wave propagates westward and suppresses the upwelling in the thermocline dome (e.g., Masumoto and Meyers 1998; Yu et al. 2005). Through this mechanism, the SWIO SST warms up and persists to the summer even as El Niño decays (Xie et al. 2002).

The SWIO warming increases atmospheric convection in the boreal spring following the El Niño (Xie et al. 2002; Annamalai et al. 2005). The intensified convection anchors an antisymmetric atmospheric circulation pattern across the equator, with northeasterly–northwesterly wind anomaly north–south of the equator. The atmospheric asymmetry is due to the SST gradient between the north and south and the reverse of the Coriolis force across the equator in the form of wind–evaporation–SST (WES) feedback (Kawamura et al. 2001; Wu et al. 2008). In the north Indian Ocean (NIO), the northeasterly wind anomaly enhances the winter monsoon in the early spring season and cools down the SST through the loss of latent heat flux. When the monsoon changes to southwesterly in May, the northeasterly anomaly sustained by the SWIO warming weakens the monsoonal wind. The reduced latent heat flux causes a second SST warming north of the equator, from the NIO to the South China Sea (SCS) (Du et al. 2009). The ocean dynamics, through reducing the Ekman transport and upwelling by weakened monsoonal wind, reinforce the SST warming in coastal regions, such as off the Somali coast in the Arabian Sea (Izumo et al. 2008) and the Vietnam coast in the SCS (Xie et al. 2003).

These processes illustrate the importance of air–sea interaction and ocean dynamics in the Indian Ocean; they are not simply a passive response to ENSO via the “atmospheric bridge” (Alexander et al. 2002). The complexity of the above processes poses a challenge for the coupled ocean–atmosphere general circulation models (CGCMs) to simulate Indian Ocean climate and SST variability. In an analysis of the World Climate Research Programme’s (WCRP) phase 3 of the Coupled Model Intercomparison Project (CMIP3) Saji et al. (2006) found that most of the models, 15 out of 17, capture the IOB-wide warming associated with ENSO with a delay of a few months. The models without the IOB mode usually have weak or wrong ENSO simulations. Although the thermocline dome in the southwestern Indian Ocean

(IO) was simulated in most models (Yokoi et al. 2009), the ocean Rossby wave propagation response to ENSO was present only in a subset of models. For example, the Geophysical Fluid Dynamics Laboratory (GFDL) model confirms that the slow propagating Rossby wave in the south TIO is the key to persisting the IOB warming into the following summer after ENSO, indicating the role of ocean dynamics in IO SST variability (Zheng et al. 2011).

The present study evaluates the simulation of the IOB mode and its relationship to ENSO in the large multimodel ensemble from phase 5 of the Coupled Model Intercomparison Project (CMIP5). It extends Saji et al.’s (2006) CMIP3 analysis not only in using the new CMIP5 ensemble (Taylor et al. 2012), but more importantly, in taking advantage of emerging results from recent studies that the IOB mode is not uniform over the TIO Basin but instead displays characteristic subbasin variations indicative of ocean–atmosphere interactions within the basin. Specifically, we examine the wind forcing of the downwelling ocean Rossby wave in December–February (DJF) (0–1) at the peak of El Niño, the development of the antisymmetric atmospheric pattern in March–May (MAM) (1), and the second peak of the NIO warming in June–August (JJA) (1). The numerals 0 and 1 denote the developing and decay years of El Niño, respectively. We show that most CMIP5 models succeed in capturing salient features and key physical processes of the IOB mode. Our results form the basis for further in-depth studies of ENSO teleconnection and internal ocean–atmosphere feedback over the TIO Basin. This is important, as recent studies show that the IOB mode provides predictability for summer climate anomalies over the NWP and East Asia (Chowdary et al. 2010, 2011).

The rest of the paper is organized as follows. Section 2 describes the CMIP5 dataset. Section 3 assesses the IOB simulation in CMIP5 models. Section 4 explores interdecadal and long term change of the IOB mode. Section 5 is a summary.

2. Data

The WCRP CMIP5 multimodel products used in this study are obtained from the Earth System Science Portals in different institutes and countries. To compare with observations, the analysis focuses on the climate of the historical runs, which are forced with the observed history of greenhouse gas (GHG) concentrations, solar radiation, and other climate forcing. At the present stage, we have obtained necessary data from 20 models. Table 1 lists the full and abbreviated names, institutions, and resolutions of the models. Monthly mean

TABLE 1. The WCRP CMIP5 models used in this study.

Model	Expansion	Source	Atmospheric Resolution	Ocean Resolution
1 ACCESS1.0	Australian Community Climate and Earth-System Simulator, version 1.0	Commonwealth Scientific and Industrial Research Organisation (CSIRO) and Bureau of Meteorology, Australia	192 × 145	360 × 300
2 BCC-CSM1.1	Beijing Climate Center, Climate System Model, version 1.1	Beijing Climate Center, China	128 × 64	360 × 232
3 CanESM2	Second Generation Canadian Earth System Model	Canadian Centre for Climate Modelling and Analysis, Canada	128 × 64	256 × 192
4 CNRM-CM5	Centre National de Recherches Météorologiques Coupled Global Climate Model, version 5	Centre National de Recherches Météorologiques/Centre Européen de Recherche et Formation Avancées en Calcul Scientifique, France	256 × 128	144 × 90
5 CSIRO Mk3.6.0	Commonwealth Scientific and Industrial Research Organisation Mark, version 3.6.0	CSIRO and Queensland Climate Change Centre of Excellence, Australia	192 × 96	192 × 189
6 FGOALS-s2	Flexible Global Ocean–Atmosphere–Land System Model gridpoint, second spectral version	Institute of Atmospheric Physics, Chinese Academy of Sciences, China	128 × 108	360 × 196
7 GFDL-ESM2G	Geophysical Fluid Dynamics Laboratory Earth System Model with Generalized Ocean Layer Dynamics (GOLD) component (ESM2G)	National Oceanic and Atmospheric Administration (NOAA)/GFDL, United States	144 × 90	360 × 210
8 GFDL-ESM2M	Geophysical Fluid Dynamics Laboratory Earth System Model with Modular Ocean Model 4 (MOM4) component (ESM2M)	NOAA/GFDL, United States	144 × 90	360 × 200
9 GISS-E2-H	Goddard Institute for Space Studies Model E2, coupled with the HYCOM ocean model	National Aeronautics and Space Administration (NASA) Goddard Institute for Space Studies (GISS), United States	144 × 90	144 × 90
10 GISS-E2-R	Goddard Institute for Space Studies Model E2, coupled with the Russell ocean model	NASA GISS, United States	144 × 90	144 × 90
11 HadGEM2-CC	Hadley Centre Global Environment Model, version 2–Carbon Cycle	Met Office, United Kingdom	192 × 145	360 × 216
12 HadGEM2-ES	Hadley Centre Global Environment Model, version 2–Earth System	Met Office, United Kingdom	192 × 145	360 × 216
13 INM-CM4.0	Institute of Numerical Mathematics Coupled Model, version 4.0	Institute of Numerical Mathematics, Russia	180 × 120	360 × 340
14 IPSL-CM5A-LR	L'Institut Pierre-Simon Laplace Coupled Model, version 5A, coupled with NEMO, low resolution	L'Institut Pierre-Simon Laplace, France	96 × 96	182 × 149
15 IPSL-CM5A-MR	L'Institut Pierre-Simon Laplace Coupled Model, version 5A, coupled with NEMO, mid resolution	L'Institut Pierre-Simon Laplace, France	96 × 96	182 × 149
16 MIROC5	Model for Interdisciplinary Research on Climate, version 5	Atmosphere and Ocean Research Institute (AORI) (The University of Tokyo), National Institute for Environmental Studies (NIES), and Japan Agency for Marine–Earth Science and Technology (JAMSTEC), Japan	256 × 224	360 × 368
17 MIROC-ESM	Model for Interdisciplinary Research on Climate, Earth System Model	AORI, NIES, and JAMSTEC, Japan	128 × 64	256 × 192
18 MPI-ESM-LR	Max Planck Institute Earth System Model, low resolution	Max Planck Institute for Meteorology, Germany	192 × 96	256 × 220
19 MRI-CGCM3	Meteorological Research Institute Coupled Atmosphere–Ocean General Circulation Model, version 3	Meteorological Research Institute, Japan	320 × 160	360 × 368
20 NorESM1-M	Norwegian Earth System Model, version 1 (intermediate resolution)	Norwegian Climate Centre, Norway	144 × 96	320 × 384

output is used, including SST, sea surface height (SSH), 10-m wind, precipitation, and sea level pressure (SLP). The historical runs span from 1870 to 2005. This study mainly focuses on the 30-yr period from 1976 to 2005, but it analyzes the multidecadal variation based on the 136-yr simulation.

For observations, we use the extended reconstructed SST (ERSST) (Smith et al. 2008) and Hadley Centre SST datasets [Hadley Centre Sea Ice and Sea Surface Temperature dataset (HadISST) and Hadley Centre Sea Surface Temperature dataset, version 3 (HadSST3)] (Rayner et al. 2003; Kennedy et al. 2011); surface winds from the monthly mean reanalysis from the National Centers for Environmental Prediction–Department of Energy (NCEP–DOE) (Kanamitsu et al. 2002), available for 1979–2008; the Hadley Centre Sea Level Pressure dataset (Allan and Ansell 2006) from 1979 to 2008; the monthly Climate Prediction Center (CPC) Merged Analysis of Precipitation (CMAP) (Xie and Arkin 1997) from 1979 to 2008; SSH from the Simple Ocean Data Assimilation reanalysis (SODA; version 2.6) from 1979 to 2008 (Carton and Giese 2008); and multisatellite altimetry observations for the period from 1993 to 2011, merged and distributed by the Collecte Localisation Satellites (CLS) Space Oceanographic Division in Toulouse, France. The mean climatological annual cycle is defined using data for the 30-yr period in models and reanalyses or the available period for satellite altimetry. Anomalies are calculated by subtracting the monthly mean values from their respective climatology. A 4–84-month Hanning bandpassing filter is applied to extract interannual anomalies, and 2-yr periods are removed from both edges before further analysis.

We perform regression and correlation analyses referenced to the Niño-3.4 (5°S–5°N, 170°–120°W) SST index averaged from November (0) to January (1) [NDJ (0–1)]. The IOB mode index is defined as SST averaged in (20°S–20°N, 40°–110°E). Note that in some figures, anomalies are the regression coefficients in field unit per degree Celsius of Niño-3.4 NDJ SST or NIO April–June (AMJ) SST anomaly, but only the field unit is given in figure captions. A *t* test is conducted on the analyses, and only the results with the statistical significance at the 90% confidence level are shown in spatial plots. To be statistically accurate for a small sample, the standard deviation across models is calculated on the Fisher transformation to stabilize the variance (Fisher 1921) and then is transformed back to correlation to represent graphically the interval of confidence, which becomes “asymmetric” (e.g., in Figs. 10 and 14b,c). The interdecadal analyses in the discussion section are based on the variance calculation and correlation in 21-yr running windows.

3. IOB mode in CMIP5 models

a. EOF modes

The basin-wide warming pattern emerges as the first EOF mode of IO SST variability, covering the entire TIO Basin as well as the SCS and the seas of Indonesia (Fig. 1); 80% of models, 16 out of 20, produce a spatial pattern similar to observations, and the rest, 4 out of 20, present an Indian Ocean dipole (IOD)-like pattern. The pattern correlation coefficients between observation and simulations have been calculated, most of them higher than 0.9 (Fig. 1). The explained variance contributions in those 16 models range from 22% to 49%, compared to 40% in ERSST (42% in HadISST; figure not shown). The second EOF mode explains variance ranging from 9% to 20%, compared to 13% in ERSST (15% in HadISST; not shown). These results are consistent with previous studies (Weare 1979; Klein et al. 1999; Saji et al. 1999, 2006; Du et al. 2009; Zheng et al. 2010, 2011). Note that the IOB mode is the second EOF mode for CSIRO Mk3.6.0, and the IOD is the first EOF mode (Fig. 1). INM-CM4.0's first EOF mode shows an IOD pattern, and the second mode (explaining 14% variance) is also IOD-like (IOB pattern correlation coefficient only 0.65). The first EOF mode in three models (ACCESS1.0, HadGEM2-ES, and MPI-ESM-LR) is IOD-like, with a negative sign off the Java coast. In Fig. 1, the composite of all models is marked as multimodel ensemble (MME) composite. Note that if the four IOD-like models are removed from the composite, the explained variance in MME increase from 32% to 34% and pattern correlation coefficients from 0.91 to 0.94. Those changes are not significant. We use an all-member ensemble mean in the following composite. The variance of principle component 1 (PC1) (PC2 in CSIRO Mk3.6.0 and INM-CM4.0), corresponding to the IOB pattern, increases in the January–July season, consistent with observations (Fig. 2). There is some model diversity in the amplitude phase locking.

In the spatial pattern of the first EOF mode, most models reproduce the maximum SST variance in the central TIO. A few models (e.g., ACCESS1.0, MPI-ESM-LR, MRI-CGCM3, and INM-CM4.0) show a maximum along the west coast of the Arabian Sea and west equatorial region, suggesting the influence of strong upwelling off the Somali coast and thermocline variation due to the downwelling equatorial Rossby wave, respectively. The maximum SST in the SWIO reaches farther west in models than that in observations, implying the impact of the downwelling equatorial Rossby wave on the thermocline and SST in the model. These models share a common cold tongue-like structure along the east equatorial region, suggesting an overestimation of upwelling

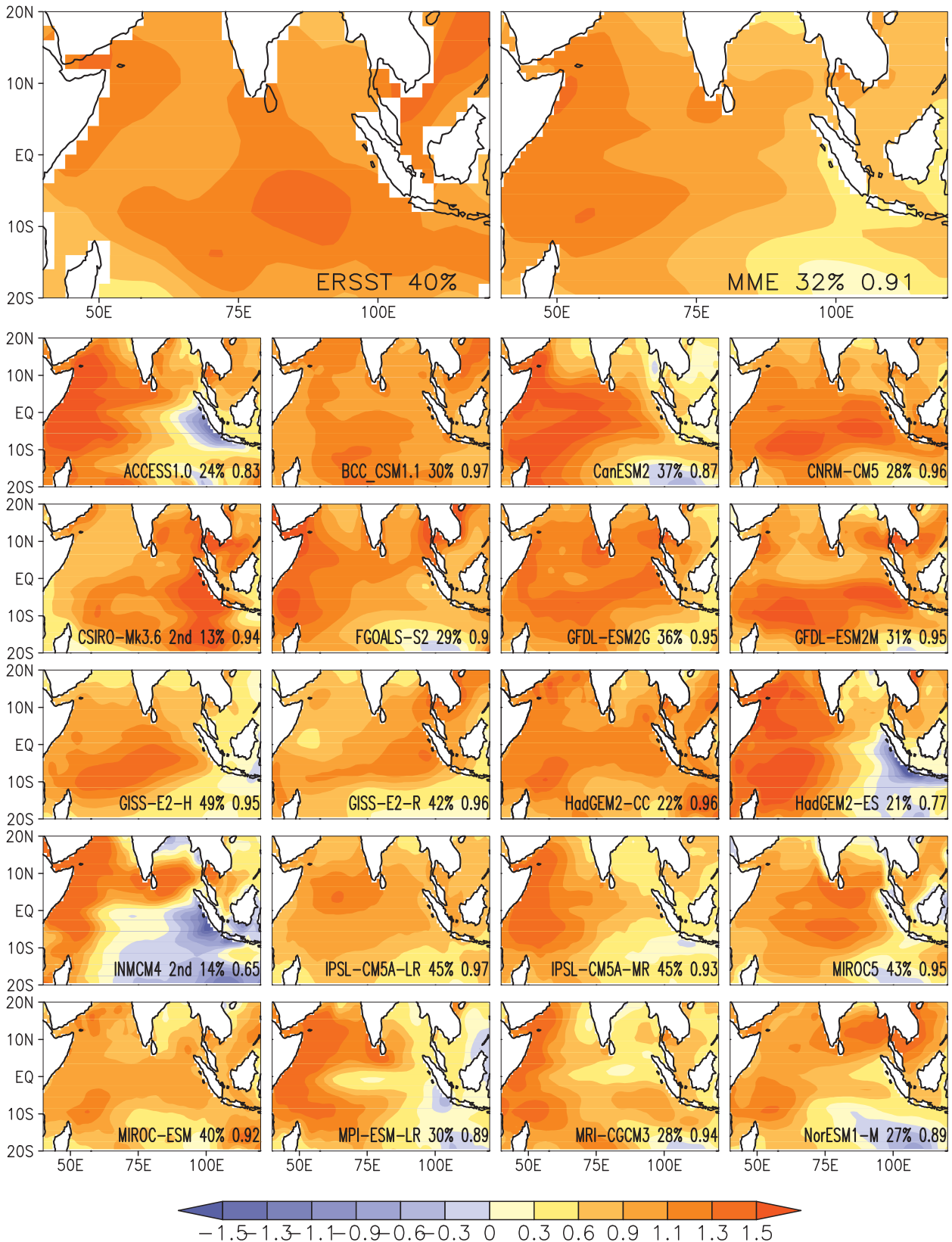


FIG. 1. First EOF modes of TIO SST variability for the models studied ($^{\circ}\text{C}$; second mode for CSIRO Mk3.6.0 and INM-CM4.0). Percentage explained variance contribution for each model and pattern correlation coefficient between ERSST and CMIP5 SST EOF modes are included in the lower-right corner of each panel. MME presents the all-models ensemble mean.

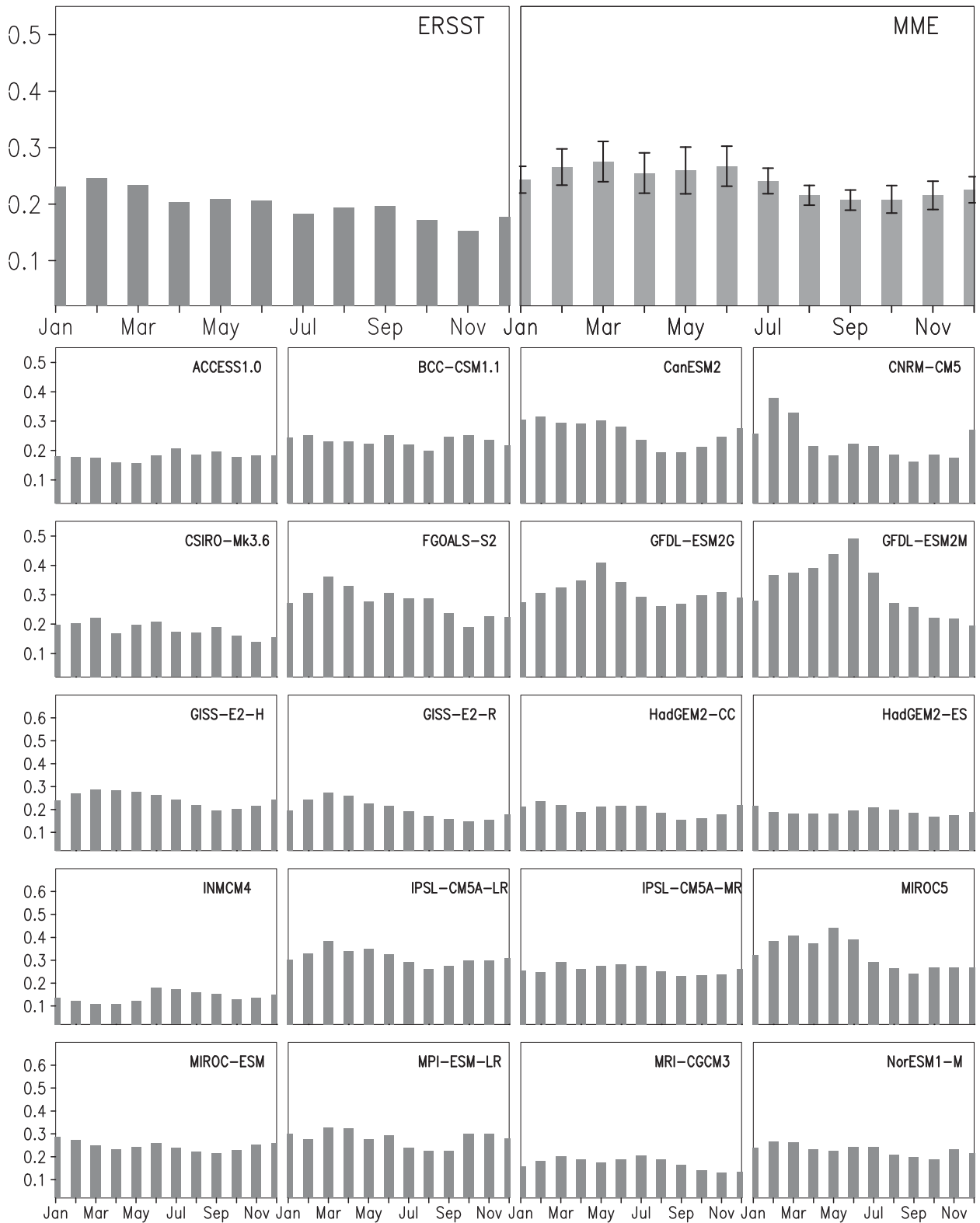


FIG. 2. Standard deviation of PC1 (PC2 in CSIRO Mk3.6.0 and INM-CM4.0) as a function of calendar month. The interval of the 95% *t*-test significance confidence level across all the models is shown in the MME plot.

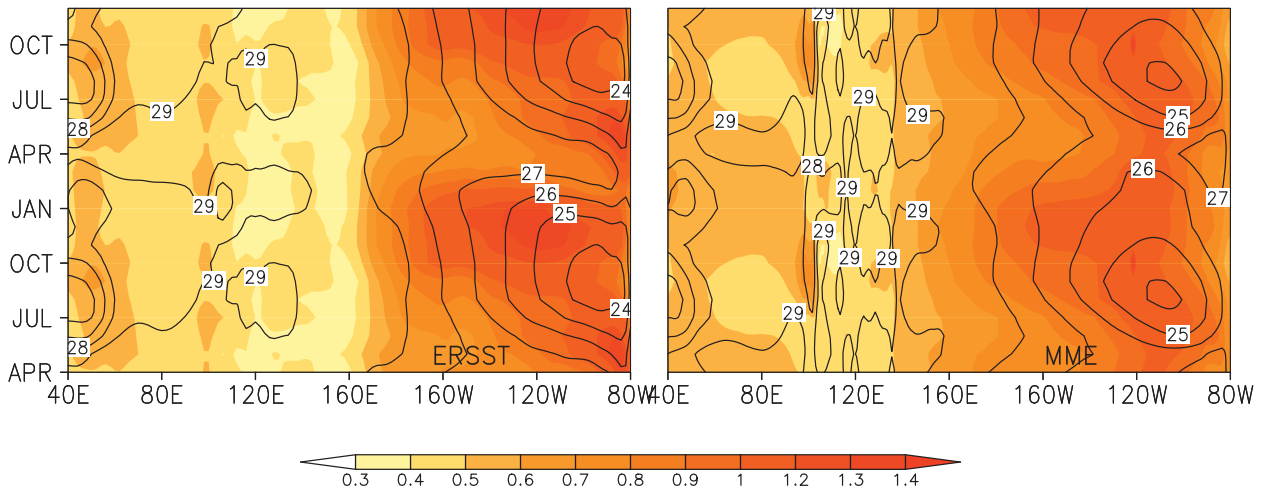


FIG. 3. Standard deviation (shading, $^{\circ}\text{C}$) of (left) ERSST and (right) MME along the equator, averaged in 5°S – 5°N , as a function of longitude and calendar month, superimposed with the seasonal cycle (contours, $^{\circ}\text{C}$).

processes off Sumatra. There, a thick barrier layer usually impedes the deep thermocline water from being entrained into the mixed layer (e.g., Qu and Meyers 2005; Masson et al. 2005), not in favor of SST variations (Du et al. 2005) except during strong IOD events (Du et al. 2008). The second EOF mode shows that these models overestimate the SST cooling off Sumatra (not shown). An ongoing study reveals the mean depth of the thermocline off Sumatra in these models is too shallow compared to observations, inducing a strong cold tongue structure (Zheng et al. 2013).

b. ENSO simulation and correlation with IOB

ENSO in the tropical Pacific is a major forcing for TIO SST variability. The simulated ENSO varies in amplitude, frequency, and pattern from model to model. Figure 3 shows the standard deviation of SST anomalies (SSTa) along the equator from the Indian to Pacific Ocean. In observations, large SST variations are located in the central and eastern Pacific, with a shift tendency of a westward propagation. The comparison with the seasonal climatological cycle indicates that the largest cooling in the CMIP5 MME is located too far away from the east Pacific coast, implying a possible discrepancy in simulating the Peru coastal upwelling. The amplitude of interannual SST variation is over 1°C in the boreal winter season in the Pacific, while in the Indian Ocean it is weaker and peaks in boreal summer season. About half of the models show a clear resemblance in the ENSO evolution to observations, while the rest still exhibit a large discrepancy (not shown). For example, the eastward propagation signature of the SST variations is mixed with a westward propagation, the maximum of SST variation shifts too far west, and the seasonality does not show a

robust phase locking as in observations. Similar issues were also noted in an earlier version of CMIP3 (e.g., Guilyardi 2006). Despite the above discrepancies, the ENSO characteristics in the multimodel ensemble are generally consistent with observations (Fig. 3). Note that the asymmetry of ENSO and IOB and their relationship are also important, are not discussed in detail in this study, and are worth further investigation in the future (e.g., An and Jin 2004; Kug et al. 2005; Ohba and Ueda 2009; Okumura et al. 2011).

The IOB mode is forced by ENSO. A scatter diagram of root-mean-square (RMS) variance (Fig. 4a), indicates that the IOB amplitude is related to that of ENSO. Half of the models simulate ENSO amplitudes comparable to observations. A Taylor diagram compares the IOB–ENSO relationship between models and observations (Fig. 4b). The correlation coefficients between IOB and ENSO in CMIP5 models range from 0.43 to 0.91, compared to 0.84 in ERSST and 0.86 in HadSST3. To avoid the influence of ENSO amplitude, the standard deviation of IOB is normalized by dividing the standard deviation of the Niño-3.4 SST index in each model (Fig. 4a). The IOB amplitude is about a quarter of that of ENSO in more than half of the models, consistent with observations. Figure 4b suggests the IOB–ENSO amplitude correlation is not related to their amplitude ratio. MIROC-ESM has the largest amplitude ratio, but its correlation with ENSO is among the smallest.

In observations, Niño-3.4 SSTa develop in AMJ (0) and decay rapidly in AMJ (1) over a 1-yr period (Figs. 5a,b). The ENSO development in CMIP5 models generally agrees with observations with 1–3 months lead-lag in a given model (Figs. 5c,e). At the decay stage, the models show much diversity. A few models transit from a positive

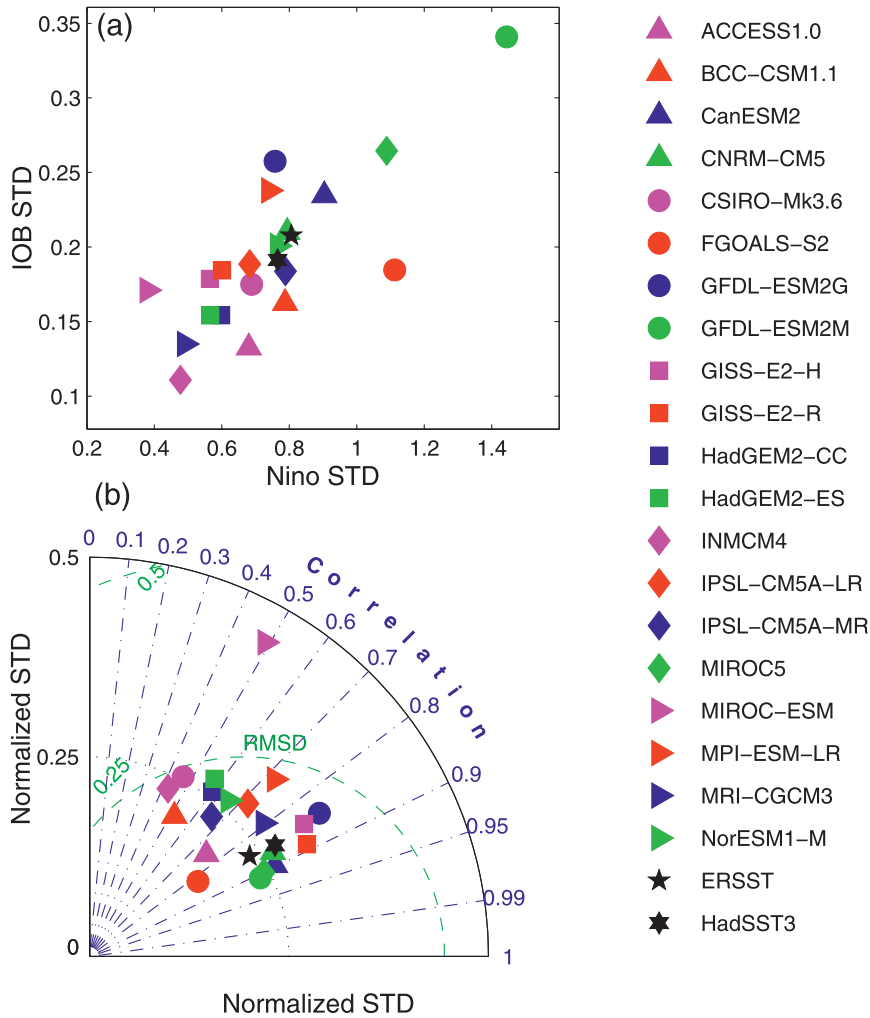


FIG. 4. Relationships of IOB and ENSO: (a) scatter diagram of standard deviations (STDs) of the TIO SST (20°S–20°N, 40°–100°E) and Niño-3.4 SST (5°S–5°N, 170°–120°W) and (b) Taylor diagram of IOB simulation. In (b), the horizontal and vertical axes denote the STD of IOB. The IOB STD is normalized by the ratio of the STD of the Niño-3.4 SST index in observations (average of ERSST and HadSST3) for each model. The outer arc is the maximum correlation between TIO SST and the Niño-3.4 NDJ (0–1) index. The green arcs denote RMS difference between the normalized IOB STD and Niño-3.4 SST STD.

to a negative event (e.g., MRI-CGCM3 and CNRM-CM5), suggesting a dominant 2-yr period (Fig. 5d). By contrast, in GFDL-ESM2M and MIROC5, the SSTa can persist longer into the July–September (1) season, possibly because of a long-lived ENSO in those models. The low autocorrelation in INM-CM4.0 suggests a high noise level in ENSO simulation. This model seems to simulate a weak air–sea interaction and weak IO variability.

TIO SST warming lags behind ENSO by 4–6 months to reach the maximum (Figs. 5a–c), and lingers into August–September (1) (Xie et al. 2009; Chowdary et al. 2012; Wu et al. 2012). Recent studies view the TIO as a capacitor (Yang et al. 2007; Xie et al. 2009). The TIO stores the heat during the development and releases the heat during the

decay of ENSO. In many models, the TIO warming persists 2–3 months longer than observations into October–November (1) (Fig. 5d), possibly because of long-lived ENSO in these models. For the long persistence of TIO warming, the second NIO warming plays an important role; 13 out of 20 models show a double peak structure in NIO warming (Fig. 5f). In 13 models, the NIO SST–ENSO correlations barely pass the 90% significance level for the February–March minimum between the two peaks, while both peaks pass the 95% significance level. Based on the Fisher (1921) transformation, we test the statistical significance for the difference between each peak and the February–March minimum. In eight (six) out of 13 models, the difference between the second (first) peak

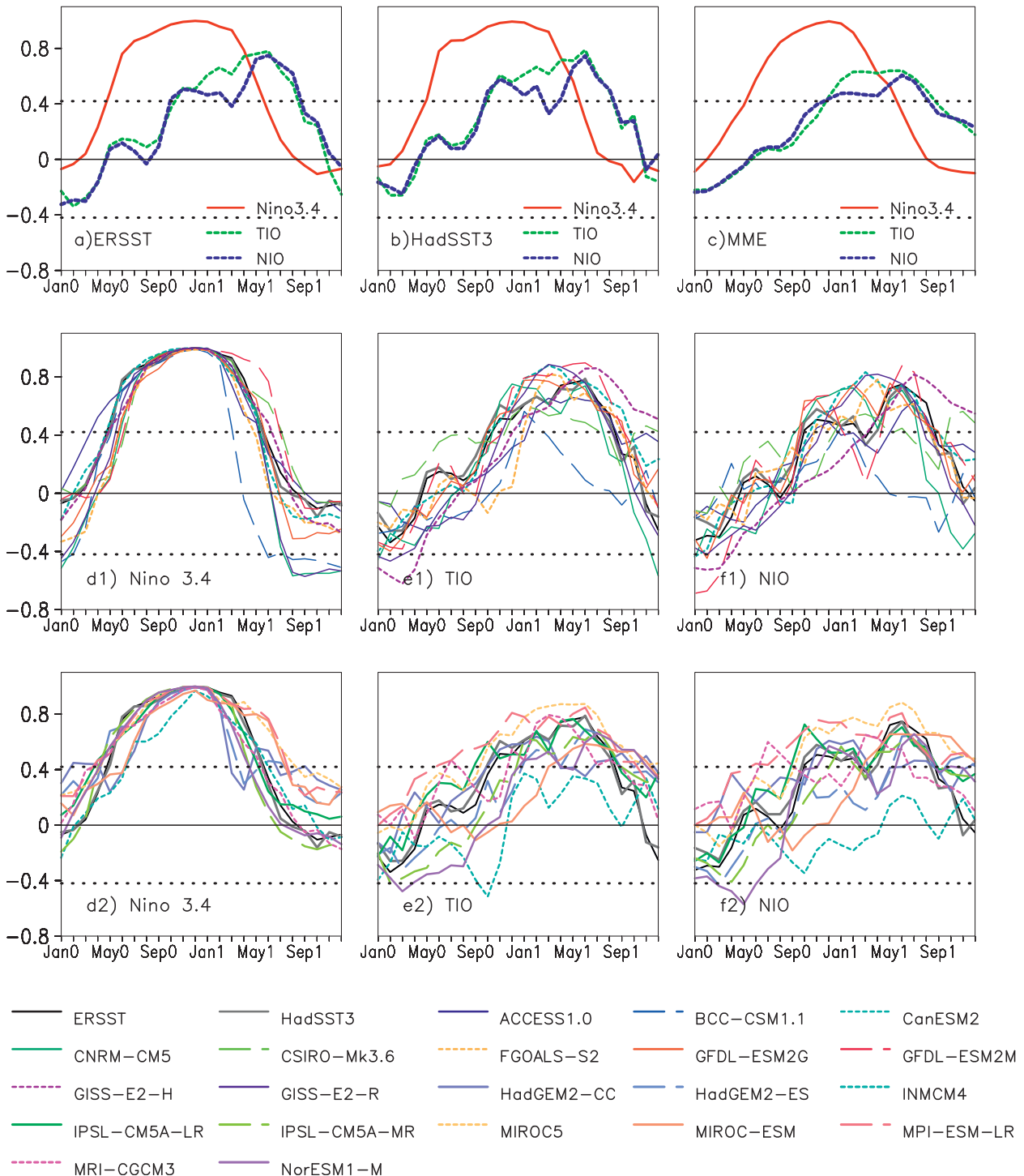


FIG. 5. Correlation of NDJ (0–1) Niño-3.4 index with: Niño-3.4 SST (5°S – 5°N , 170° – 120°W ; red solid line), TIO SST (20°S – 20°N , 40° – 100°E ; green dashed line), and NIO SST (0° – 20°N , 40° – 100°E ; blue dashed line) based on the (a) ERSST, (b) HadSST3, and (c) all-model composite. Also shown are the correlations of Niño-3.4 NDJ (0–1) SST index with (d) Niño-3.4 SST (5°S – 5°N , 170° – 120°W), (e) TIO SST (20°S – 20°N , 40° – 100°E), and (f) NIO SST (0° – 20°N , 40° – 100°E); Items in (d)–(f) are shown in two panels (e.g., d1 and d2) so that the individual models may be better seen. The dotted black line denotes statistical significance at a 95% t -test confidence level.

and minimum passes the 95% (90%) significance confidence level, consistent with observations. Thus, the double peak structure is significant in about a half of the models. Previous studies found that the second peak of NIO warming involves internal air–sea interaction within the TIO and is the key for the TIO warming to persist into the following summer (Du et al. 2009).

c. Atmospheric forcing over the southeast TIO

During the development phase of El Niño, an anomalous high-pressure system develops over the Maritime Continent as part of the Southern Oscillation (Wallace et al. 1998; Wang et al. 2003). The change of atmospheric convection induces anticyclonic wind anomalies over the SEIO (Fig. 6). During the September–November (SON) (0) season, the northeast flank of the anticyclonic atmospheric circulation favors surface evaporation, vertical mixing, coastal upwelling, and thus, SST cooling off Sumatra and Java (Shinoda et al. 2004). The southwest flank weakens the trade wind in the central south Indian Ocean and warms the SST (Yu and Rienecker 1999). Along with the slowdown of the Walker circulation, the suppressed convection over and west of Sumatra and Java decrease precipitation over the region (Yamagata et al. 2004).

Most models simulate the anticyclonic circulation over the SEIO. The results have been normalized by the ratio of the standard deviation of Niño-3.4 SST in observations to models. Similar normalization has been made for other variables in the following figures. Particularly, the simulated anticyclonic circulation occupies the entire south TIO in the MME composite. Associated SST cooling and abnormal precipitation extend into the central equatorial Indian Ocean. The deviations of the simulation from observations may lie in the departure of ENSO simulation in the Pacific. In many models, ENSO (Figs. 3, 6) extends to 130°–150°E, about 20°–40° longitude too westward compared to observations. Note that the anticyclonic atmospheric circulation in some models is not phase locked in the SON season. Take GISS-E2-H as an example: the appearance of the anticyclonic atmospheric circulation is delayed by 1–2 months, a consequence of the diversity of model ENSO (Figs. 5d–f).

At the mature phase of El Niño (Fig. 7), in the SEIO, the prevailing wind shifts to northeasterly, a change important for the development of interannual anomalies (Nicholls 1984; Klein et al. 1999; Shinoda et al. 2004; Ohba and Ueda 2009). The northeast flank of the anticyclonic atmospheric circulation, particular in the region west of Sumatra and Java, weakens, and so do the coastal upwelling and surface evaporation (Murtugudde et al. 2000). Together with the increased solar radiation due to suppressed convective clouds, the SST in the SEIO switches from negative toward positive in the following

season (Tokinaga and Tanimoto 2004). In the southwest flank of the anticyclonic atmospheric circulation, the reduced trade winds enhance the SST warming by decreasing latent heat flux release. The precipitation increase extends southeastward from the west TIO to the central south Indian Ocean.

Most models capture the anticyclonic atmospheric circulation in DJF (0–1), with similar SST and precipitation patterns to observations. Particularly, the east–west contrast of rainfall pattern reflects the Walker circulation reduction during the mature phase of El Niño (Wang and Picaut 2004). A few models (e.g., GFDL-ESM2G, HadGEM2-ES, MRI-CGCM3, and MPI-ESM-LR; figure not shown) overestimate the atmospheric circulation in the NIO or easterly wind along the equator. The signature seems an extension of the anticyclonic atmospheric circulation over the NWP, as part of atmospheric Rossby waves induced by local negative SSTa at the ENSO mature phase (Wang et al. 2000; Wang and Picaut 2004). This circulation causes SST warming to withdraw to the west (Fig. 7) (also refer to Xie et al. 2009 and Huang et al. 2010). The westward extension of the anticyclonic atmospheric circulation over the NWP seems related to the ENSO structure that is displaced westward compared to observations in the equatorial region (K. Hu et al. 2013, personal communication).

d. Oceanic Rossby wave in the south TIO

In the SON (0) and NDJ (0/1) seasons, the anticyclonic atmospheric circulation over the SEIO forces and strengthens downwelling Rossby waves that propagate westward. The SST warming copropagates with the oceanic Rossby wave (Xie et al. 2002; Du et al. 2009). SSH anomaly (SSHa) reaches the maximum in April (1) (Fig. 8), whereas SST anomaly peaks in May–June (1) (Fig. 9a). The 1–2-month delay in the SST response is due to the annual shoaling of the thermocline in June–July (Fig. 9b) (Perigaud and Delecluse 1993; Masumoto and Meyers 1998), which enhances thermocline feedback. The interannual depression of the shallow thermocline reduces the cold upwelling water into the mixed layer and increases the SST, which explains why the surface heat flux is not important for the SST warming during the May–June (1) season (Klein et al. 1999; Yokoi et al. 2012). The Rossby wave–induced warming over SWIO affects the atmosphere in this period (Xie et al. 2002; Annamalai et al. 2005; Schott et al. 2009). Precipitation increases during February–June (1), with the maximum in April (1) (Fig. 9c), which prolongs the annual precipitation in this season (Fig. 9d).

In Fig. 8, half of models reproduce the Rossby wave propagation, with some differences in position and phase. Convection anomaly seems related to the Rossby wave in

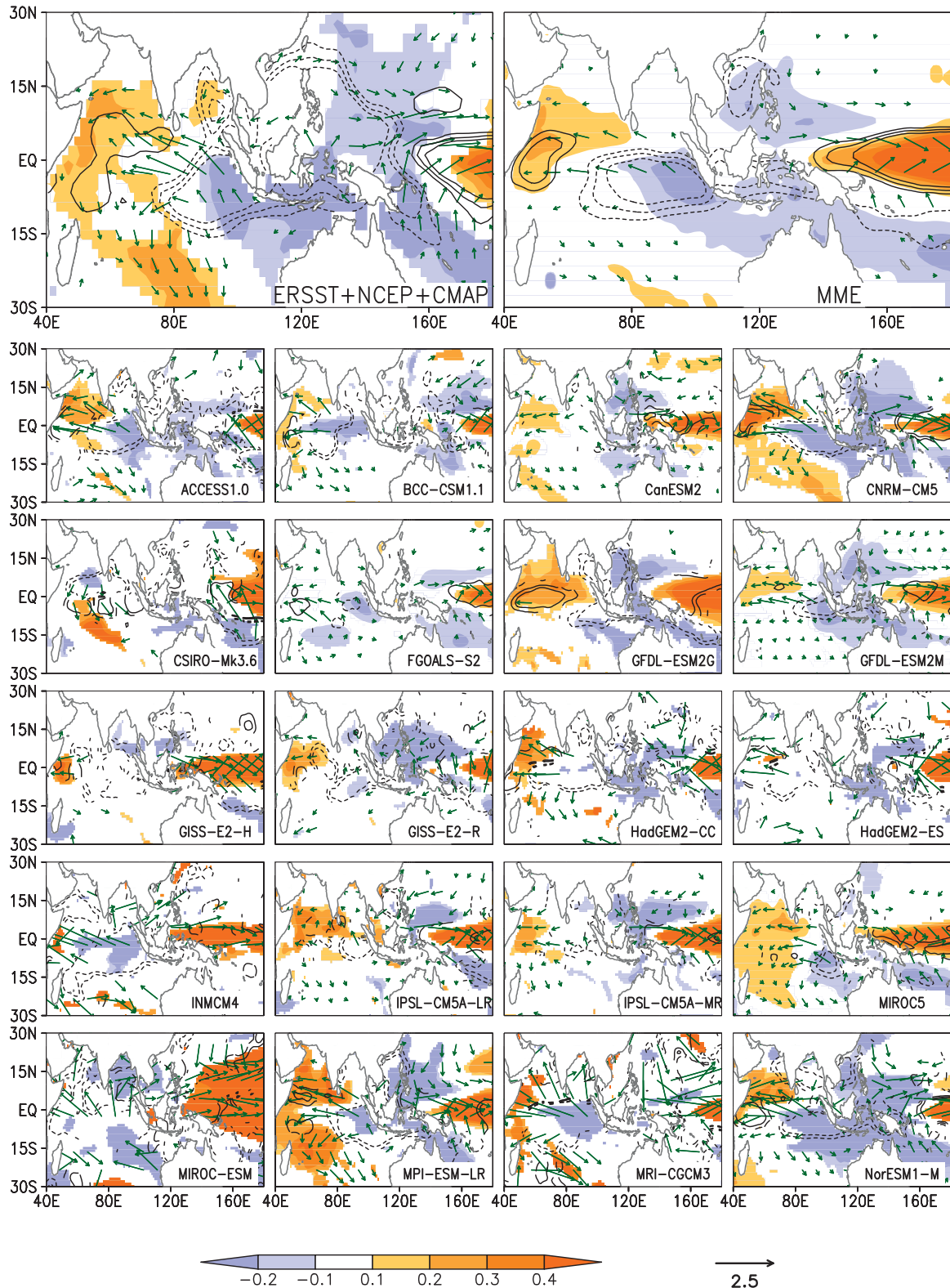


FIG. 6. Regression of the NDJ (0–1) Niño-3.4 index with SON (0): SST (color shading, $^{\circ}\text{C}$), surface wind (vectors, m s^{-1}), and precipitation [contours, contour interval (CI) = 0.3 mm day^{-1} , starting from $\pm 0.6 \text{ mm day}^{-1}$] at an over 90% t -test confidence level.

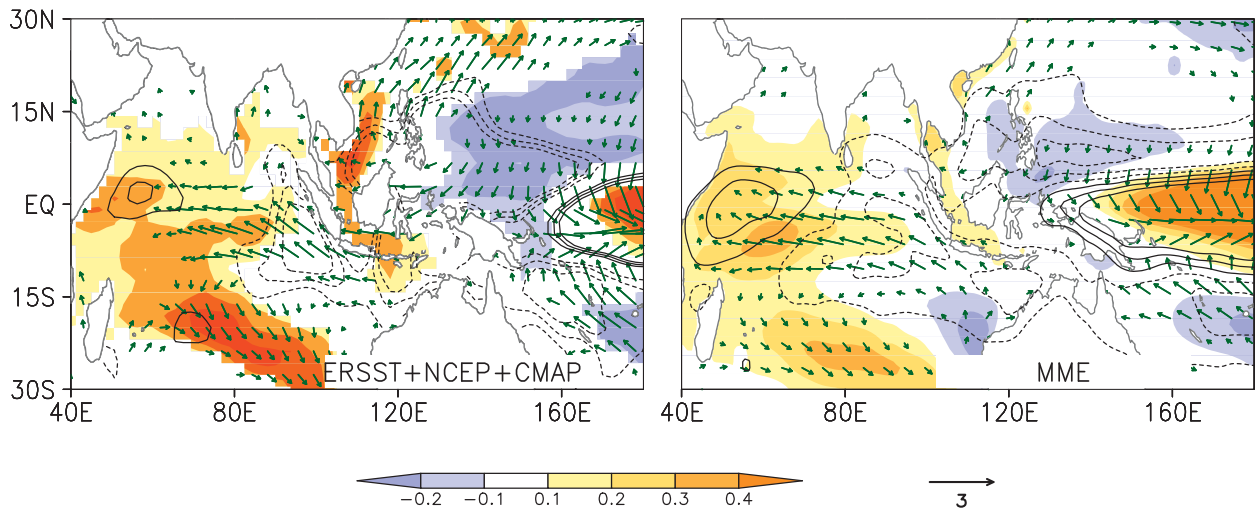


FIG. 7. As in Fig. 6, but to DJF (0–1) and only for the top two panels.

these models. Abnormal precipitation activities occur over the south TIO in the decay phase of ENSO. The difference of models from the observed SSHa may be related to the simulation of the seasonal cycle of the thermocline depth and anticyclonic atmospheric circulation in the south TIO. For the models without robust Rossby wave propagation, the precipitation anomalies are not well simulated in location, phase, or amplitude, implying the importance of ocean dynamics for climate in the south TIO. An exception is GFDL-ESM2M, in which Rossby wave shows no propagation but air–sea interaction is among the most pronounced in all the models. The significant thermocline deepening in GFDL-ESM2M is due to the strong forcing by the in situ anticyclonic atmospheric circulation. Consistently, abnormal precipitation in GFDL-ESM2M occupies the entire south TIO during February–June (1). This process suggests that the change in the thermocline ridge can be caused either by the incoming Rossby wave adjustment or the local wind curls. The thermocline ridge is fundamental to the ocean-induced atmospheric change over the south TIO. Figure 9 shows that in models the SST warming appears in the upwelling season of the thermocline. Most of the models show a close relationship between SSTa and SSHa in the SWIO during MAM (1) (Figs. 10, 11). Only a few models have problems in this SST–thermocline feedback, either without showing a depressed thermocline following El Niño or mismatched anomalies in location or phase (e.g., BCC-CSM1.1; Fig. 8).

e. WES feedback and antisymmetric atmospheric circulation

In the boreal spring following El Niño, the increased SST warming intensifies convection and, thus, precipitation

over the south TIO, particularly in the west (Fig. 11), whereas the SST warming weakens and precipitation decreases to the north over the NIO and SCS. Consistent with the SST and convection pattern, surface wind anomalies feature an antisymmetric circulation structure, with northeasterlies north and northwesterlies south of the equator. This C-shaped wind pattern is a result of the Coriolis force acting on the northerly cross-equatorial winds to induce an easterly (westerly) component north (south) of the equator.

Previous studies suggested that the antisymmetric atmospheric circulation pattern results from WES feedback in the TIO (Kawamura et al. 2001; Wu et al. 2008; Du et al. 2009). The WES feedback helps to maintain a meridional SST gradient across the equator under the favorable easterly background wind (Xie and Philander 1994). During the early spring over the SWIO thermocline ridge, the northwesterly anomalies weaken the prevailing southeasterly trade winds, sustaining the SST warming. In the NIO the northeasterly anomalies, as part of the WES mode north of the equator, strengthen the northeasterly background wind and contribute to the reduction of the SST warming over the Arabian Sea (Du et al. 2009).

Some CMIP5 models suggest that the antisymmetric atmospheric circulation is forced by anomalous positive SST and enhanced convection in the south TIO (Fig. 11; e.g., GFDL-ESM2G, and HadGEM2-CC), which in turn are maintained by the deepened thermocline ridge (Figs. 8 and 11), as in observations. In a few other models, the wind anomalies are easterly in the eastern/southeastern equatorial Indian Ocean (Fig. 11) because of the El Niño–induced Walker circulation slowdown, obscuring the C-shaped wind (Fig. 12). Eight out of 20

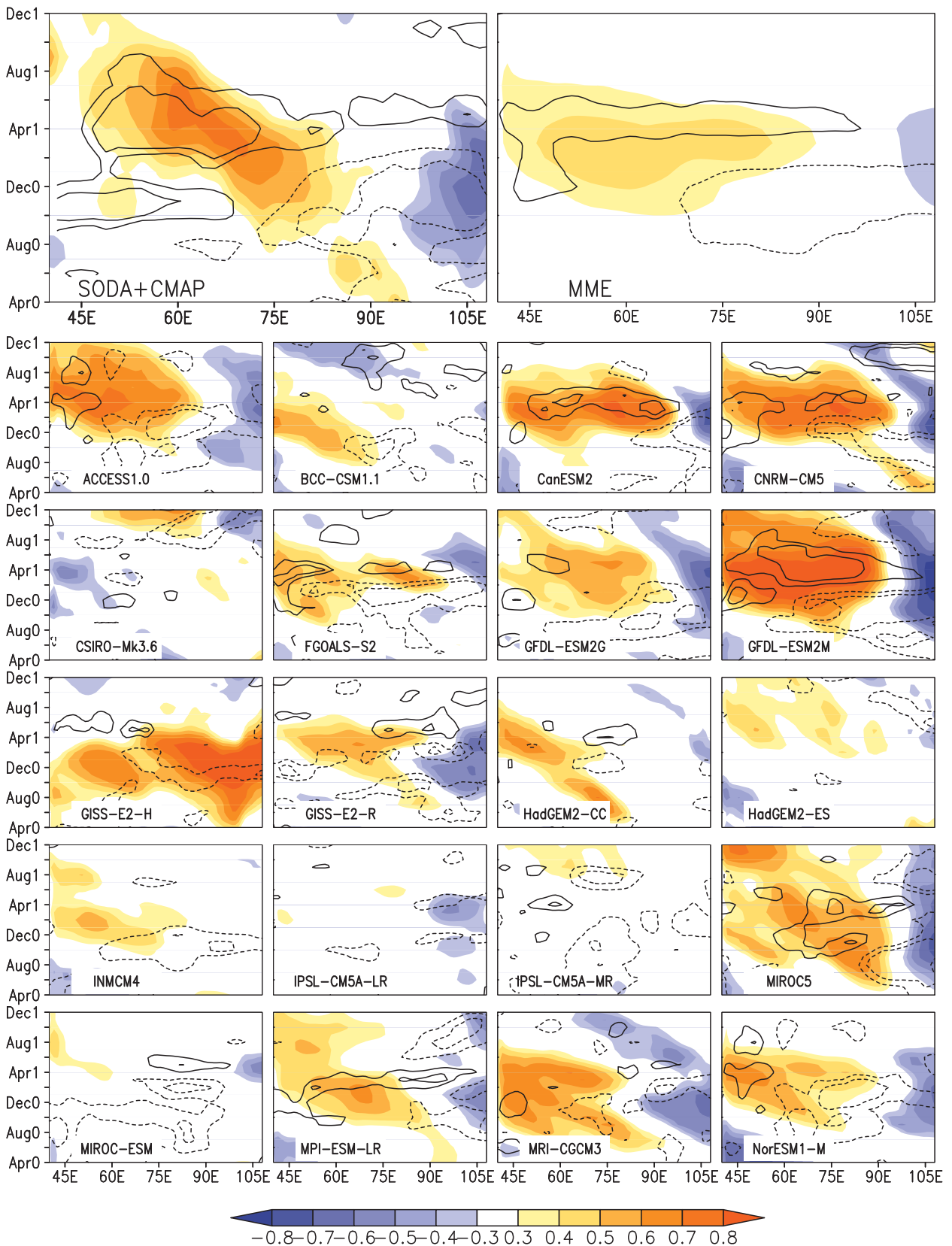


FIG. 8. Longitude-time section of model correlations with the NDJ (0-1) Niño-3.4 index: SSH (color shading) and precipitation (contours, CI = 0.2, starting from ± 0.3) averaged over 8° - 12° S.

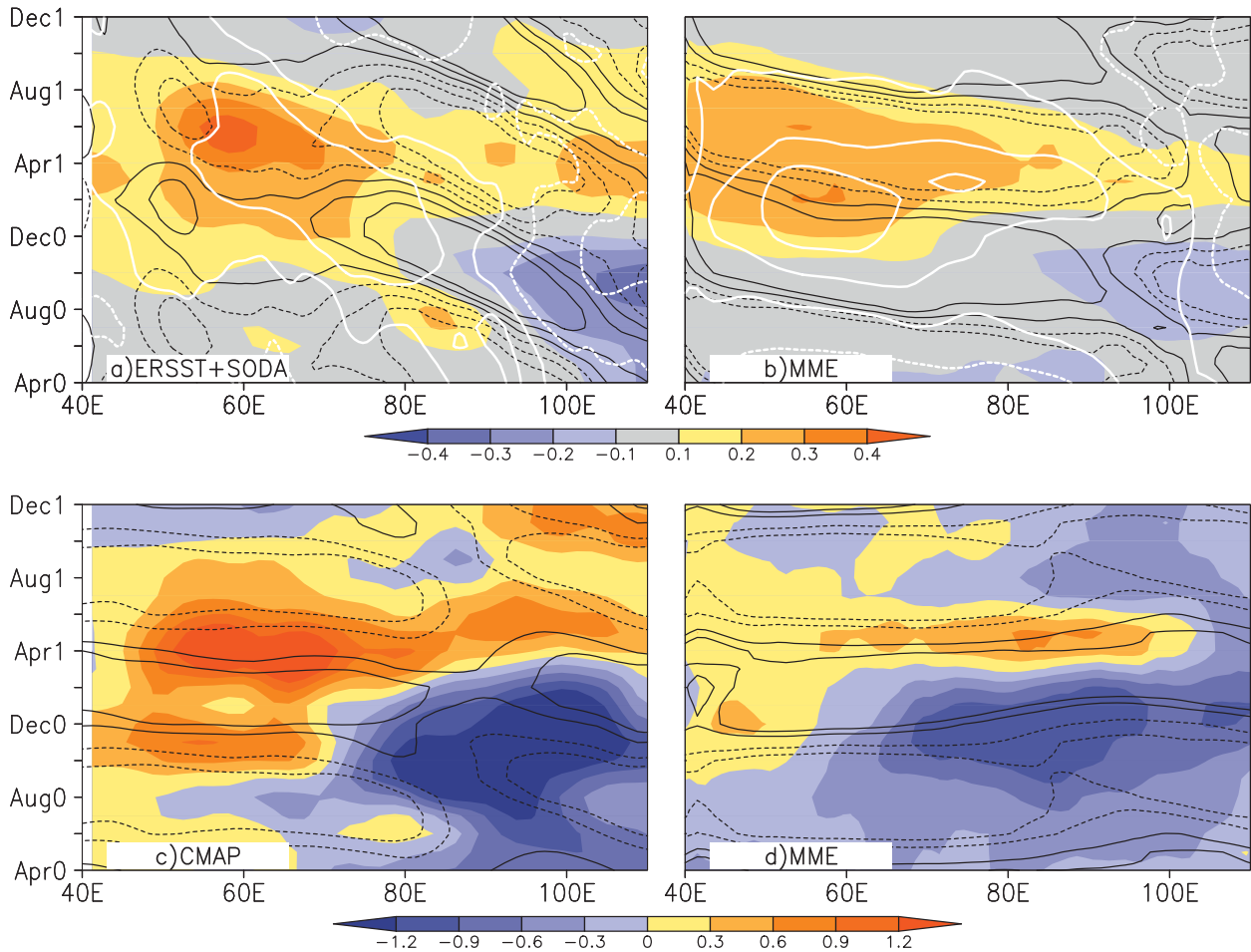


FIG. 9. Longitude–time sections averaged over 8° – 12° S: (a) ERSST + SODA; (b),(d) MME; and (c) CMAP. (a),(b) SST (color shading, $^{\circ}$ C) and SSH (white contours, CI = 2 cm, starting from ± 1 cm) each expressed as regressions with the NDJ (0–1) Niño-3.4 index; and SSH seasonal climatology (black contours, CI = 2 cm, starting from ± 1 cm). (c),(d) Precipitation (color shading, mm day^{-1}) expressed as a regression with the NDJ (0–1) Niño-3.4 index; and precipitation seasonal climatology (black contours, CI = 0.9 mm day^{-1} , starting from $\pm 0.9 \text{ mm day}^{-1}$).

models present the relationship between antisymmetric SST and wind anomalies across the equator (Fig. 12, upper-right quadrant), indicating a WES feedback. The wind circulation pattern is anticyclonic south of the equator (Fig. 11), forcing SSHa–thermocline depth anomalies (Fig. 8). The anticyclonic wind circulation reduces the upwelling over the thermocline ridge, sustaining the SST warming (Figs. 9–11).

f. NIO second warming and anticyclonic atmospheric circulation over NWP

In the NIO and SCS, wind anomalies remain northeasterly until early summer following El Niño. Because of the mean winds change from northeasterly to southwesterly in April–May, the northeasterly anomalies weaken the summer monsoonal winds, reducing the release of latent heat flux in favor of the SST warming in JJA (1) (Fig. 13). On the other hand, the change of

upwelling further amplifies the SST warming in the west Arabian Sea (Izumo et al. 2008) and west SCS (Xie et al. 2003; Jing et al. 2011). The SWIO SST warming weakens as the Rossby wave propagates to the west boundary region and decays. The most pronounced atmospheric anomalies are the anticyclonic circulation over the NWP. Xie et al. (2009) showed that the TIO warming impacts on the NWP through the baroclinic atmospheric Kelvin wave from the TIO. In the NWP, this equatorial Kelvin wave induces atmospheric divergence near the surface north of the equator and thus triggers suppressed convection and the anomalous anticyclonic atmospheric circulation in the summer following El Niño.

In 15 out of 20 models the SST warming in AMJ (1) is related to the reduction of the southwest monsoonal wind in the NIO (Fig. 14a). Note the weakening winds further reduce the Ekman transport and upwelling, especially in the Somali coastal region (Izumo et al. 2008).

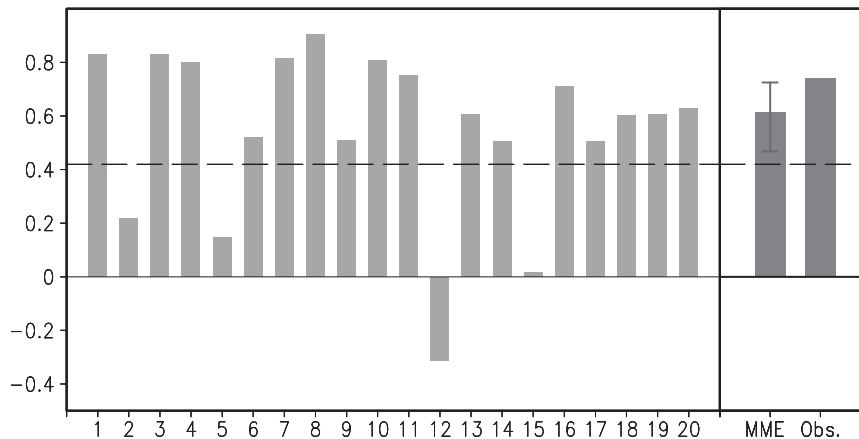


FIG. 10. The correlation between SSHa and SSTa averaged in SWIO (15° – 5° S, 55° – 75° E) during the MAM season for 20 models. Dark gray bars at right present the 20 models' ensemble mean and observations. Numbers along the x axis are for the models listed in Table 1. Dashed line denotes statistical significance at the 95% t -test confidence level. Error bar in MME gives the range of 1 standard deviation across the models. The 95% confidence interval level across the models is marked in the MME panel, which is calculated on the Fisher transformation of the correlation (Fisher 1921).

The reduction of latent heat flux release is highly correlated with the SST warming in the NIO in 11 models because of the reduced monsoonal winds, especially the zonal wind component (Figs. 14b,c). Most models reproduce the NIO warming and anomalous NWP anticyclonic circulation in JJA (1) (Fig. 13), suggestive of their connection. Half of the models simulate the contrast between the negative SLP in TIO and positive SLP anomalies in NWP as in observations. The increase in precipitation in TIO forces a Kelvin wave response with low pressure and easterly wind anomalies along the equator, which triggers a reduction in precipitation and the formation of the anticyclonic circulation over the NWP. Previous model experiments (Xie et al. 2009) showed that the SSTa over the NIO are important to the position and pattern of the anomalous anticyclonic circulation over the NWP.

g. Time–latitude variations along IO

Figure 15 shows the Hovmöller diagram of SST, wind, and SLP for observations and models. Data are zonally averaged in 40° – 80° E to avoid large diversity among models over the east TIO. Similar to observations, the simulated SST warming persists for nearly 10 months from December (0) to August (1). In NIO, simulated SST warming decays faster than observations and is mostly confined south of 15° N, whereas it extends to 25° N in observations. The SST warming in the south Indian Ocean is much stronger in the model. The easterly wind anomaly along the equator is stronger in models, indicative of the reduced Walker circulation and overextended anticyclonic wind circulation in the south TIO

in the CMIP5 models (Figs. 6, 7). The anomalous anti-symmetric wind in boreal spring is weak in models. The negative anomaly in SLP appears twice in observations, in October–November (0) and April–September (1), whereas it only occurs once in August–September (1) in models. The northward propagating tendency of SST, wind, and SLP in observations is not obvious in some of the models; ACCESS1.0, CanESM2, GISS, GFDL, IPSL, and MPI-ESM-LR models show such a northward propagation.

4. Discussion

ENSO exhibits variations on decadal time scales (e.g., D'Arrigo et al. 2005; Bunge and Clarke 2009). The coral proxy data and tree-ring records (Urban et al. 2000; Li et al. 2011) and in situ SST observations (e.g., Bunge and Clarke 2009) since the 1870s illustrate the change of frequency and strength of ENSO on long time scales. The coral proxy data show that ENSO variability intensifies with shorter periods of less than 2.9 yr from the late nineteenth to the early twentieth century, weakens with 5–7 yr during the 1920s–50s period, and enhances again and features a period of approximately 4 yr after the 1960s (Urban et al. 2000). The RMS variance in a 21-yr sliding window exhibits amplitude changes in the 1920s and 1960s (Fig. 16). ENSO regains the strength in the late 1970s, which is comparable to the early 1900s, consistent with previous studies (e.g., An and Wang 2000). Although the sparse sampling and noise level bring uncertainty in low frequency variations before 1950s (e.g., Gershunov et al. 2001), the independent works support the existence

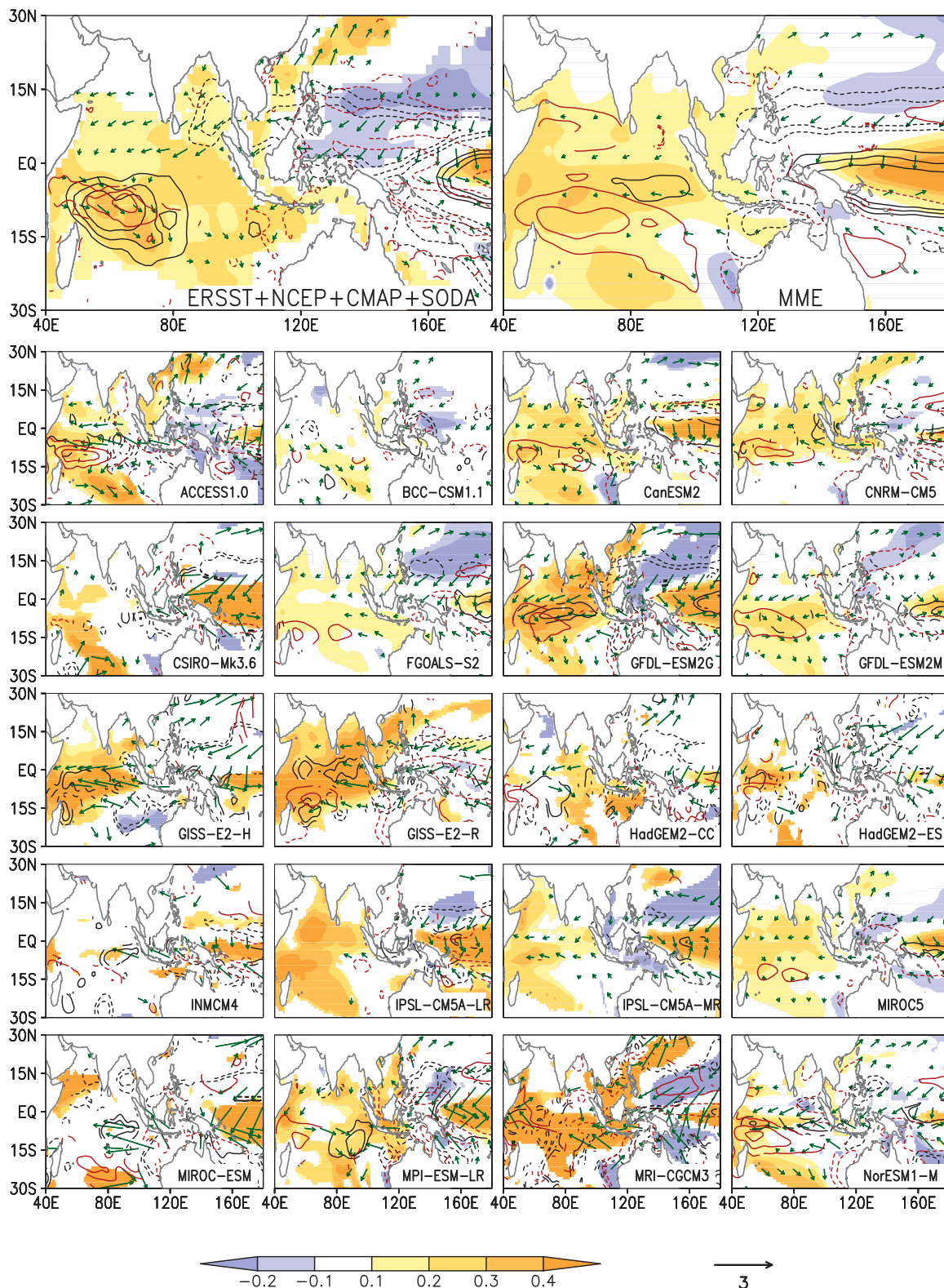


FIG. 11. Regression of the NDJ (0–1) Niño-3.4 index with MAM (1): SST (color shading, °C), surface wind (vectors, m s^{-1}), sea level height (red contours, CI = 2 cm, starting from ± 2 cm), and precipitation (black contours, CI = 0.6 mm day^{-1} , starting from $\pm 0.3 \text{ mm day}^{-1}$) at an over 90% t -test confidence level.

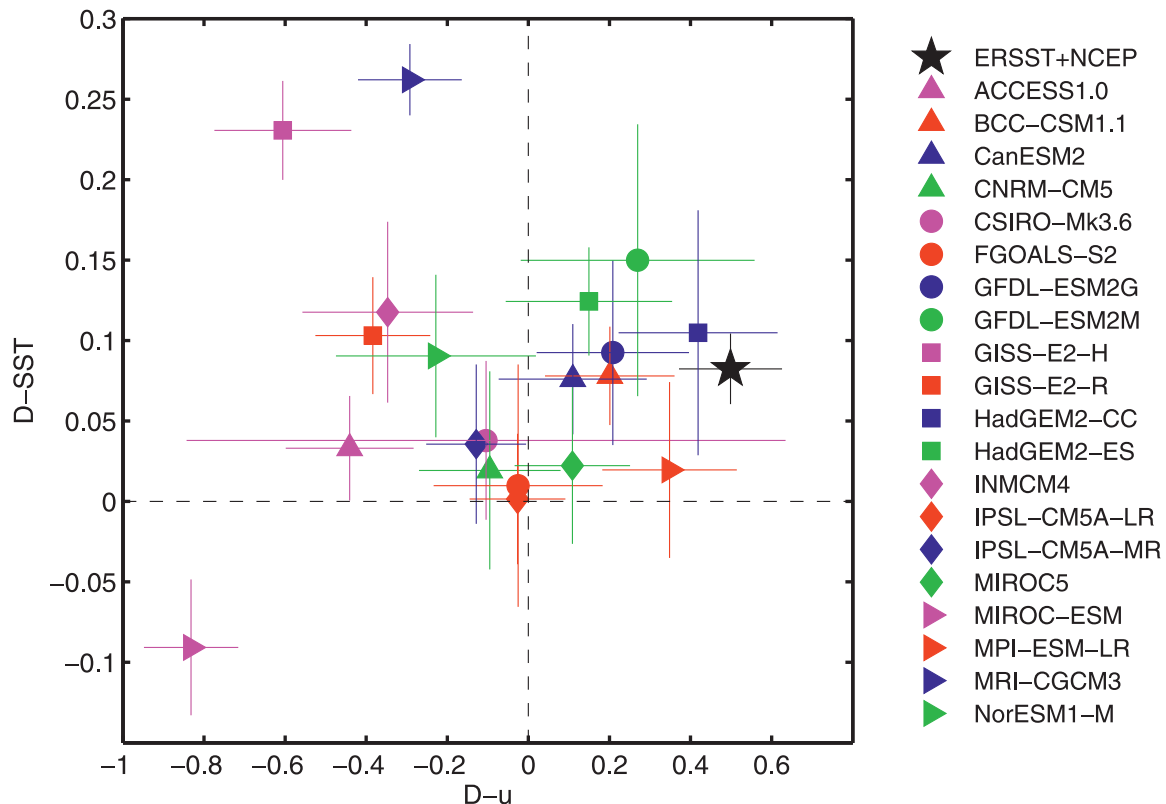


FIG. 12. Scatter diagram of the relationship of the models between zonal wind anomalies and SSTa of SIO (0° – 15° S, 50° – 100° E) minus NIO (0° – 15° N, 50° – 100° E) in MAM (1). Error bars show the 1 standard deviation range.

of decadal modulations of the strength of ENSO (e.g., Urban et al. 2000; Bunge and Clarke 2009; Deser et al. 2010). In the entire instrumental record, ENSO is phase locked to the NDJ (0–1) season. Studies based on the CMIP3 product suggested that the recent energetic ENSO may be related to the global warming, as the Pacific changes toward warmer and wetter conditions (Meehl et al. 2007). The change reflects a shift to a lower mean Southern Oscillation index (SOI) value and a flattening thermocline in the equatorial Pacific (Power and Smith 2007; Yeh et al. 2009) due to the weakening of the Walker circulation along the equatorial Pacific (Vecchi et al. 2006; Tokinaga et al. 2012). A subject of debate, the enhanced warming in the Pacific Ocean, common to model projections of future climate (e.g., Liu et al. 2005; Xie et al. 2010; Meehl et al. 2007), remains to be validated by instrumental and paleoclimate observations (e.g., Collins et al. 2010). In particular, high-quality observations suggest an intensification of the Walker circulation and a La Niña-like SST trend in the last two decades (Feng et al. 2011; Merrifield and Maltrud 2011; Li and Ren 2012), probably due to a rapid warming in the Indian Ocean (Luo et al. 2012).

Global coupled GCMs simulate strong interdecadal to centennial modulations of ENSO (e.g., Wittenberg

2009). Indeed, in CMIP5, many models display multi-decadal variability in ENSO amplitude, but the phases are not consistent with observations, suggesting the importance of internal variability. Figures 16 and 17 show results from four representative models.

The multidecadal ENSO modulations affect the IOB variance. Xie et al. (2010) found that the IOB mode intensifies after the decadal shift in the mid-1970s. Figure 16 confirms it and shows another IOB intensification in the late nineteenth to early twentieth century (Chowdary et al. 2012), though the data sampling is limited in the early period. In those four models, the ENSO amplitude determines IOB variance (Fig. 16).

The ENSO–IOB correlations vary on interdecadal time scales (Fig. 17), related to the strength and persistence of ENSO. In observations, ENSO amplitude is the weakest during the 1940s–60s, when the IOB correlation with ENSO is the smallest. Figure 18a illustrates the relationship between ENSO amplitude and ENSO–IOB correlation in the JJA (1) season during the entire period of the historical run. Increased ENSO variance corresponds to an enhanced ENSO–IOB correlation in models (Fig. 18a). A similar relationship exists for the IOD response to ENSO decadal modulations (Izumo et al. 2013). For each model, the decade with the maximum

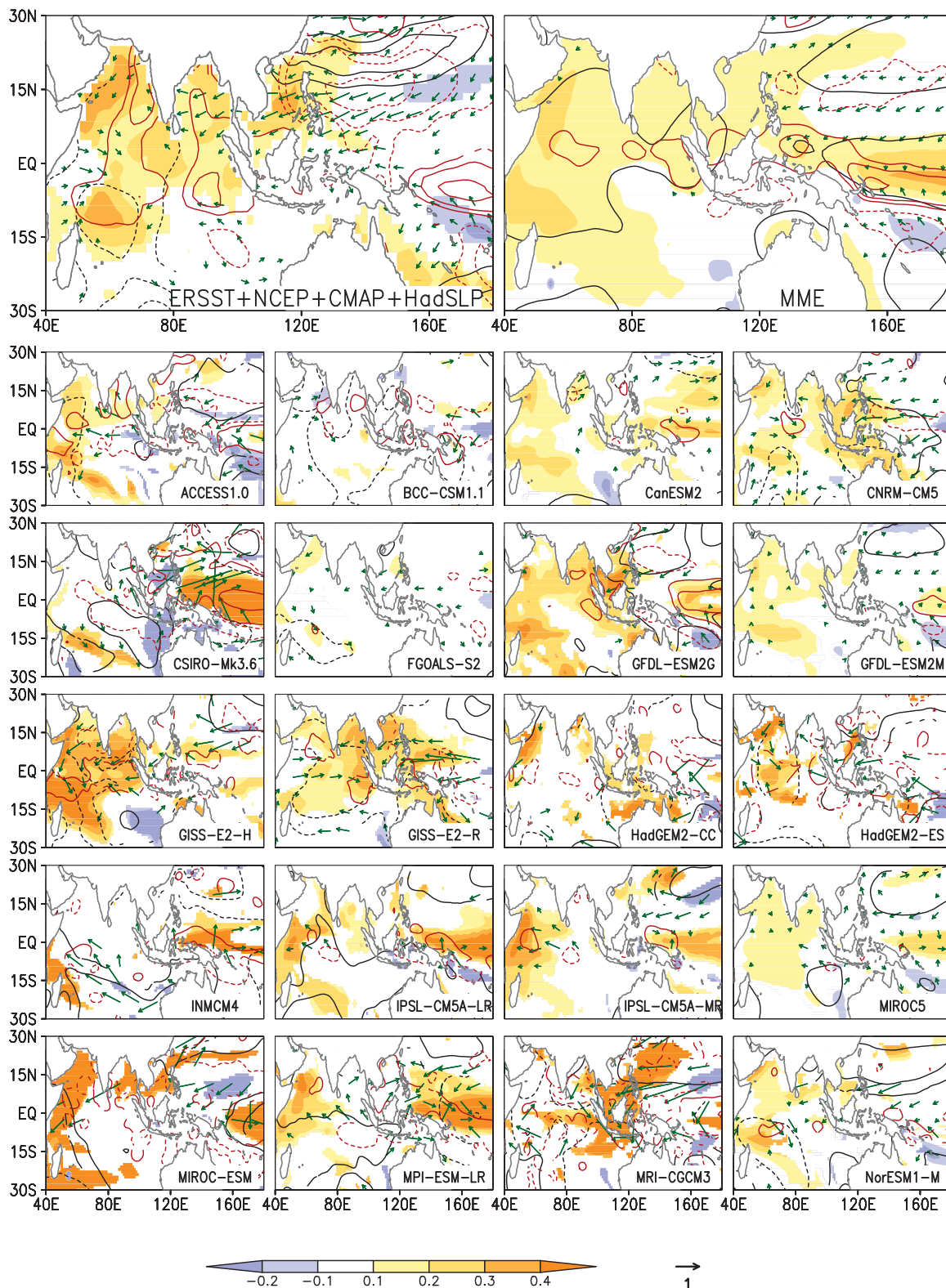


FIG. 13. Regression of the NDJ (0–1) Niño-3.4 index with JJA (1): SST (color shading, °C), surface wind (vectors, m s^{-1}), precipitation (red contours, $\text{CI} = 0.3 \text{ mm day}^{-1}$, starting from $\pm 0.3 \text{ mm day}^{-1}$), and SLP (black contours, $\text{CI} = 0.1 \text{ hPa}$, starting from $\pm 0.4 \text{ hPa}$) at an over 90% t -test confidence level.

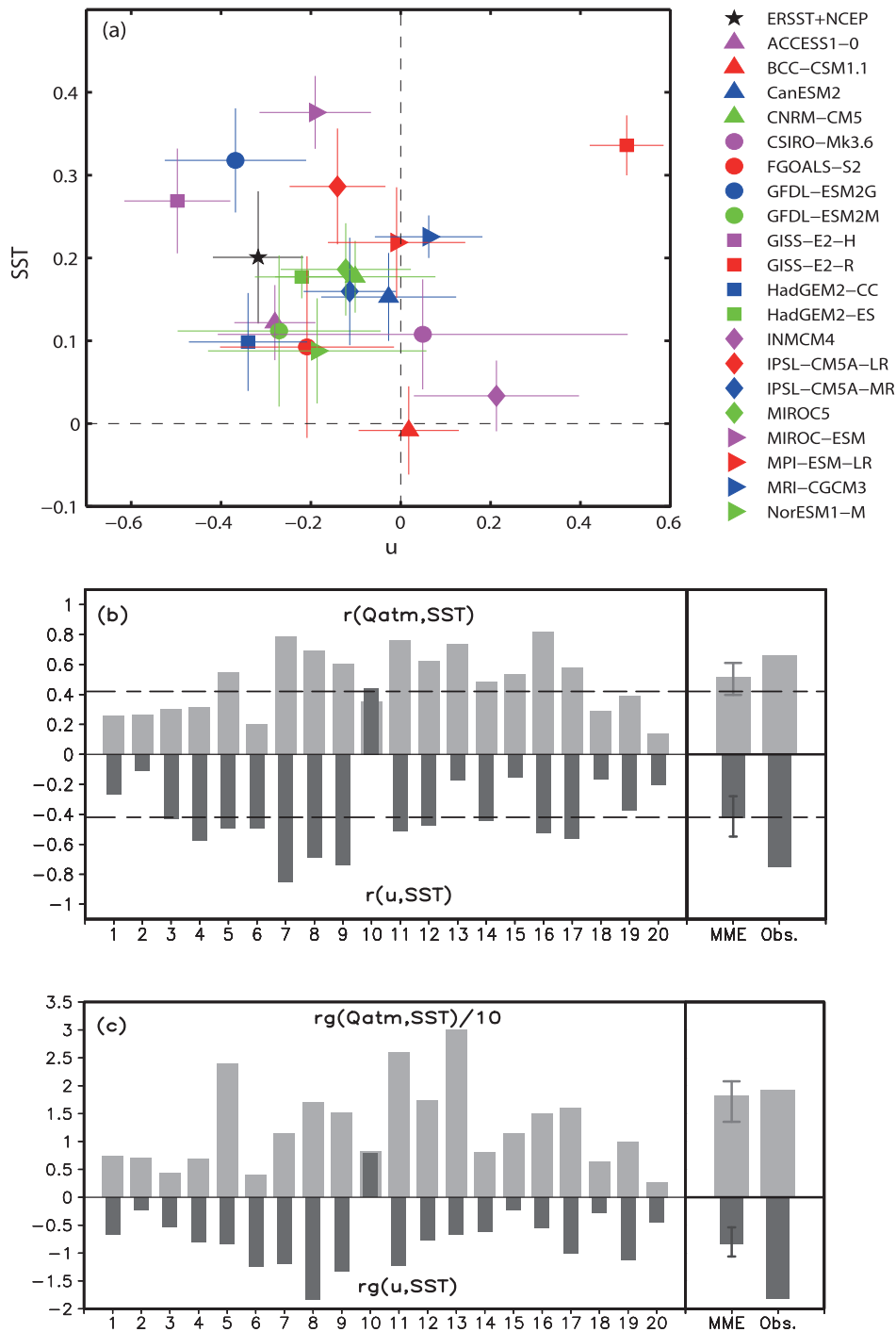


FIG. 14. (a) Scatter diagram of the relationship between the zonal wind anomaly ($m s^{-1}$) and SSTA ($^{\circ}C$) in NIO (0° – $15^{\circ}N$, 50° – $100^{\circ}E$) in AMJ (1). Q_{atm} is defined as the atmospheric forcing component in the latent heat flux, due to atmospheric adjustments in wind speed, relative humidity, and surface air–sea temperature difference, defined as the latent heat flux minus the Newtonian cooling term (Du et al. 2009) (b) Correlation between both Q_{atm} and zonal wind anomaly, and SSTA in NIO (0° – $15^{\circ}N$, 50° – $100^{\circ}E$) in AMJ (1) for 20 models. (c) As in (b), but for regression with Q_{atm} regression on SSTA divided by 10 for better portrayal. Numbers on the x axis in (b),(c) indicate the models listed in Table 1. Dashed lines in (b) denote statistical significance at the 95% t -test confidence level. In (b),(c), the 95% confidence level interval across all the models is shown in the MME panel, which is calculated on the Fisher transformation of the correlation (Fisher 1921).

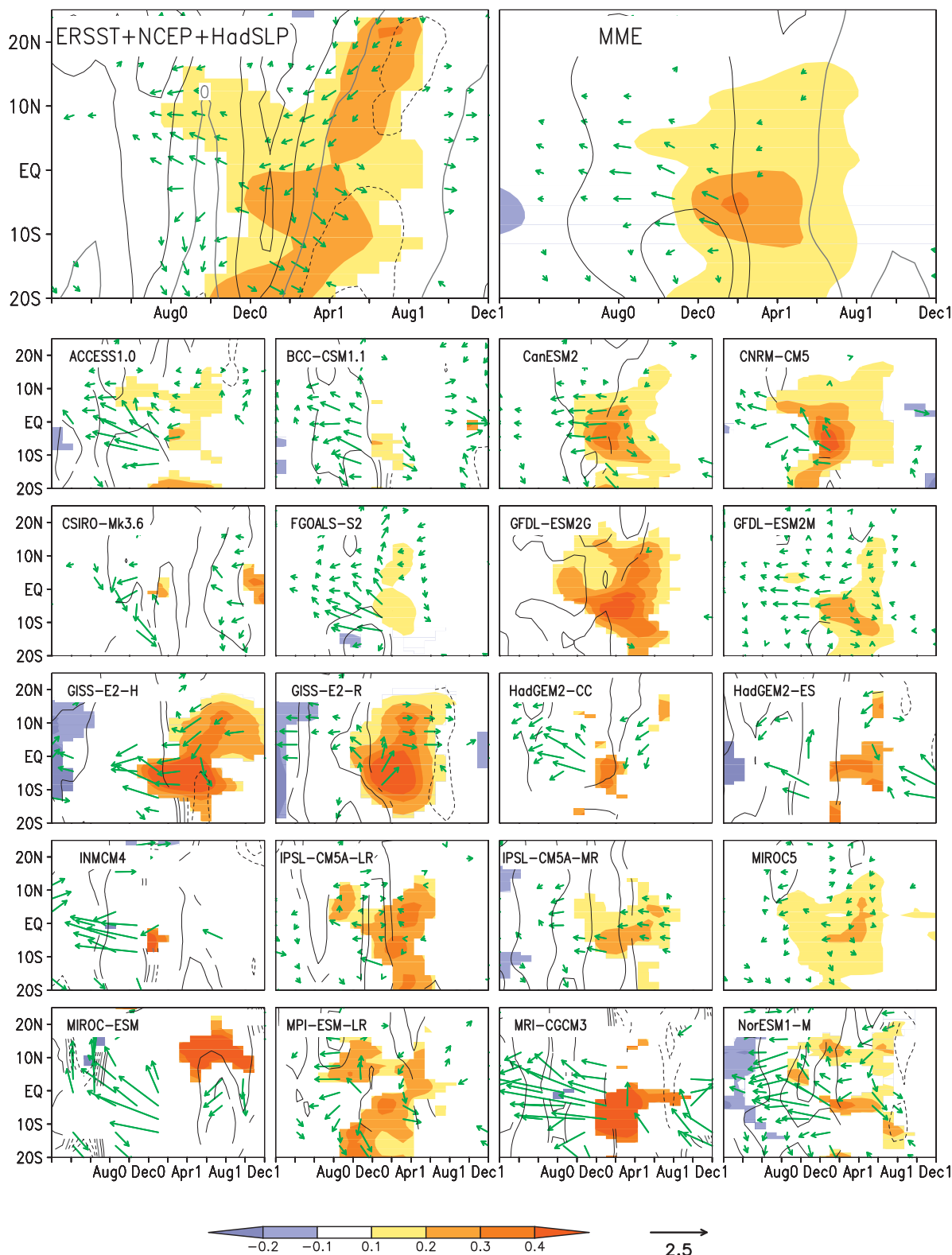


FIG. 15. Regressions of NDJ (0–1) Niño-3.4 index as a function of calendar month and latitude with SST (color shading, °C) averaged over TIO (40°–100°E), surface wind (vectors, m s^{-1}) averaged over 40°–80°E, and SLP averaged over 40°–80°E (contours, CI = 0.2 hPa) at an over 90% t -test confidence level.

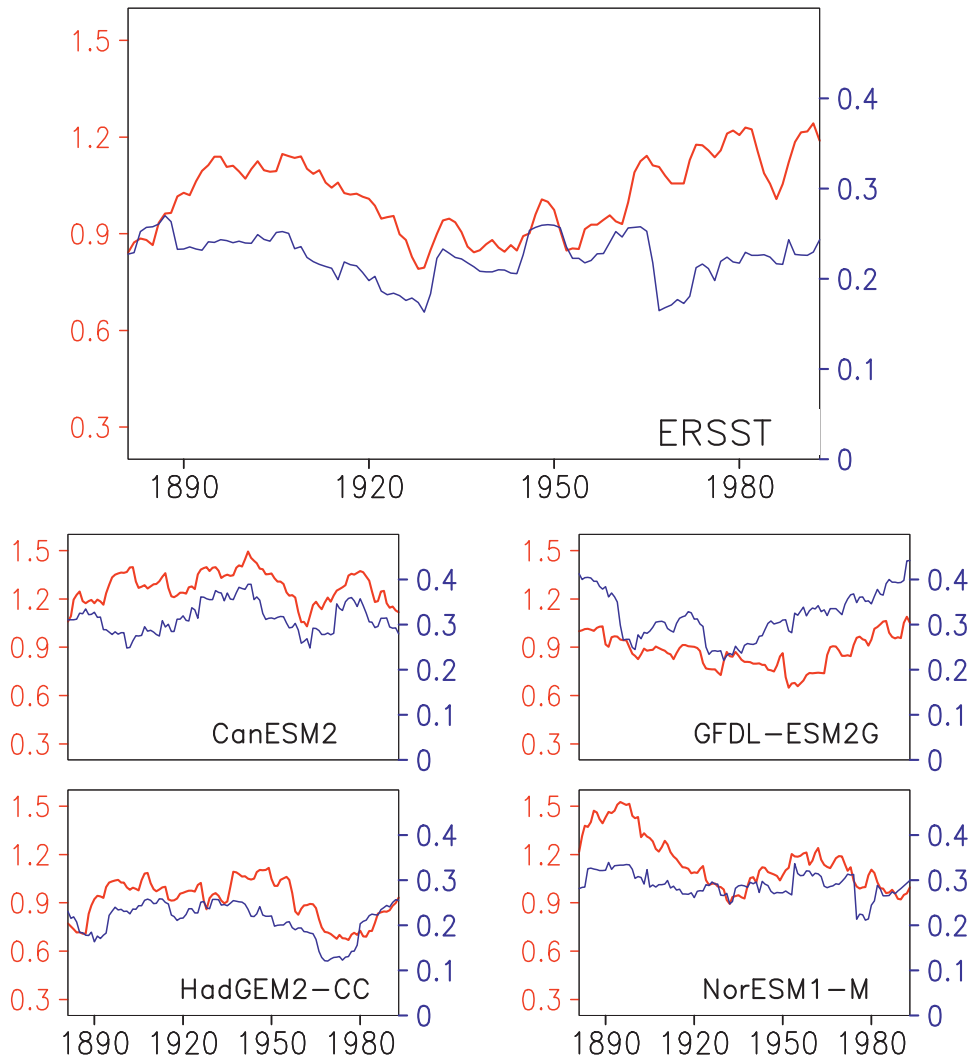


FIG. 16. The 21-yr running STD of Niño-3.4 NDJ (red line) and TIO May–July SST indices (blue line) for the models listed.

correlation is compared with the decade with the minimum correlation (Fig. 18b). In almost all models, the correlation is low when ENSO variance is low, suggesting that the ENSO variances control the ENSO–IOB correlation in the JJA (1) season. The relationship between IOB and ENSO strength is not only confirmed in intermodel difference (Fig. 18a) but also in each individual model (Fig. 18b). The result also demonstrates the model diversity in simulating the natural decadal variability.

We examine the interdecadal variations of the IOB mode in further detail, using GFDL-ESM2G. Figure 19 shows the IOB evolution in three epochs, according to the decadal variation in TIO warming (Fig. 17). A late TIO warming in 1956–75 results from a strong cooling in the SEIO in the DJF (0/1) season, related to the strong anticyclonic circulation over the SEIO. In epochs of 1926–55 and 1975–2005, the meridionally antisymmetric

wind anomalies are well developed in MAM (1). The IO warming in those epochs have different impacts on the NWP anticyclonic circulation during the subsequent summer. The strong anticyclonic circulation during JJA (1) in 1976–2005 is associated with the warming in the Bay of Bengal and SCS, while the atmospheric anomalies are weak in 1926–55, as the NIO warming is weak. The differences in the three epochs illustrate the role of low-frequency ENSO modulation in TIO and NWP climate variation. A companion work discusses show modulation of NWP climate variability in detail (K. Hu et al. 2013, personal communication).

5. Summary

We have evaluated the IOB mode simulation in 20 CMIP5 models against observations. In 16 out of 20

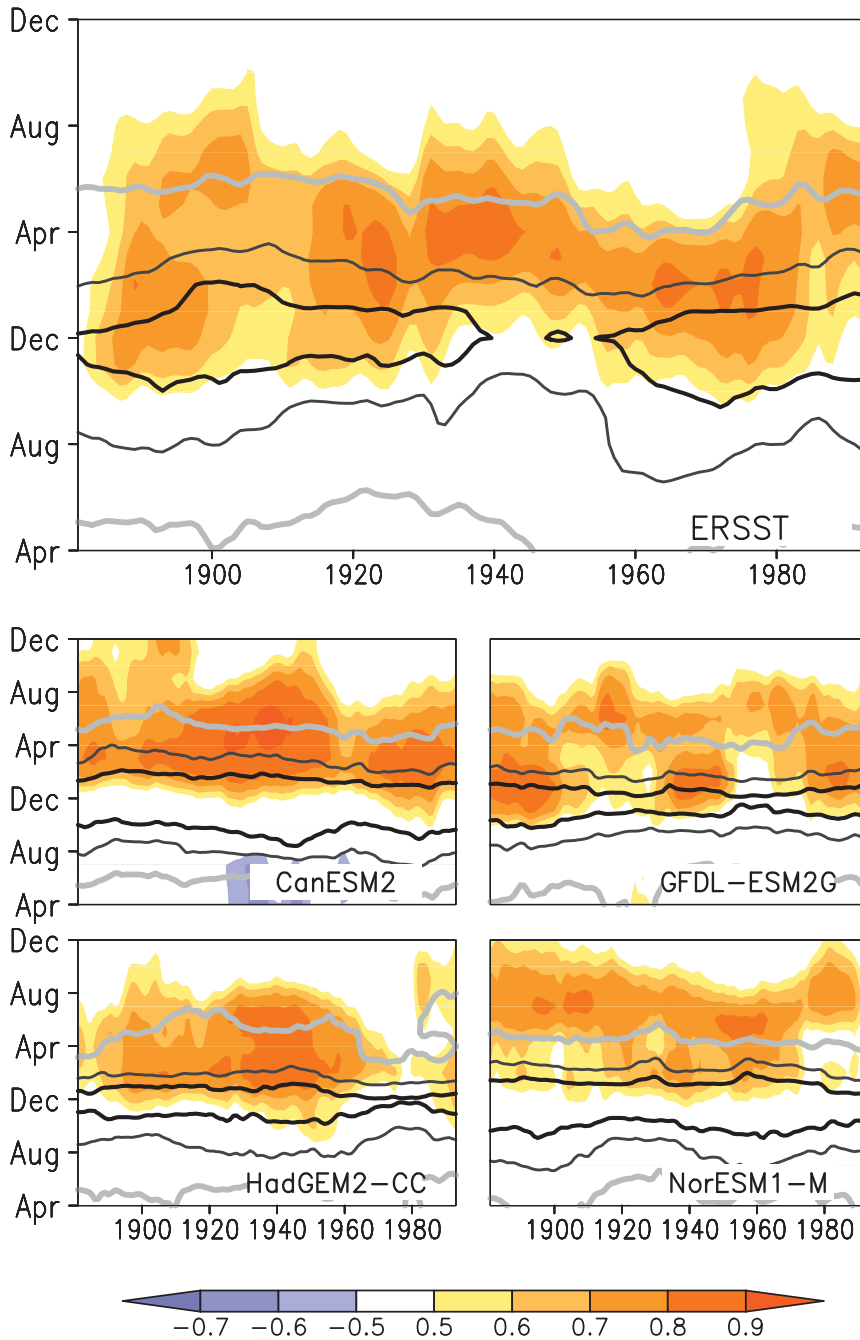


FIG. 17. The 21-yr running correlation of the NDJ (0–1) Niño-3.4 index for the models listed with TIO (color shading) and Niño-3.4 SST (contours; light gray, dark gray, and black lines show 0.5, 0.9, and 0.975, respectively).

models, the IOB is well simulated. Among them, the IOB mode contributes about 22%–49% RMS variance (40% in observations). In most models, the IOB mode is highly correlated with ENSO. The IOB mode in the MME starts from November (0) of the ENSO developing year [October (0) in observations] and terminates roughly the

same time as in observations [August (1)], with 0–3-month variations in timing in individual models. The north Indian Ocean (NIO) warming can persist into the summer following El Niño. CMIP5 simulations show that the TIO warming is not uniform but has a pronounced geographic distribution, a feature not well documented

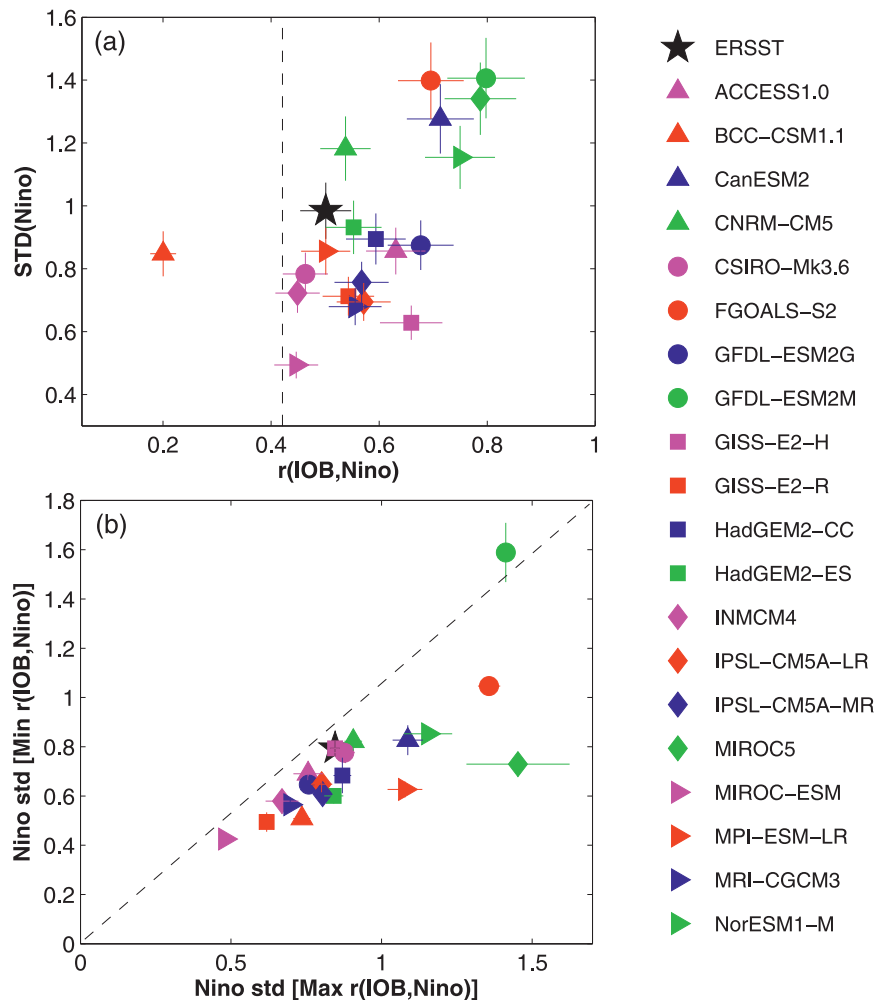


FIG. 18. Scatter diagrams of (a) the correlation (r) between NDJ (0–1) Niño-3.4 with JJA (1) IOB indices [$r(\text{IOB}, \text{Niño})$] against standard deviation of NDJ (0–1) Niño-3.4 index [$\text{STD}(\text{Niño})$] and (b) $\text{STD}(\text{Niño})$ during decades when $r(\text{IOB}, \text{Niño})$ reaches the maximum against that during decades when $r(\text{IOB}, \text{Niño})$ reaches the minimum (analysis covers 1870–2005). The standard deviation and correlation are calculated in 21-yr running windows. Error bars show 1 standard deviation ranges.

before but consistent with observations. Ours represents the first CMIP study examining the development of the IOB's geographic patterns that are due to local ocean–atmosphere interactions.

Some models simulate the antisymmetric atmospheric circulation across the equator in boreal spring, a key aspect of IOB development. The antisymmetric atmosphere anomalies peak in MAM (1) but may be delayed by 1–2 months in some models. South TIO SST is the forcing of this atmospheric pattern in observations, triggered by the oceanic Rossby wave forced in prior seasons over the central and eastern TIO. In most CMIP5 models, the anomalous wind forcing covers the full zonal extent of the south TIO. For models without a clear Rossby wave

propagation, the in situ anomalous wind curls deepen the thermocline to sustain the SST warming in the south TIO.

SSTa over NIO persist into summer. In some models, the SST warming over the NIO and SCS exhibits a second peak in the El Niño decay summer, suggesting the effect of TIO–atmosphere interaction. In most models, the NIO warming in summer is associated with reduced surface heat flux out of the ocean associated with the reduced southwest monsoonal wind, a result consistent with the previous heat budget analysis in observations (Du et al. 2009). A further heat budget analysis is required in the future to quantify this effect compared to other possible factors in CMIP5 models. Particularly, there might be regional differences among NIO subbasins (Montégut

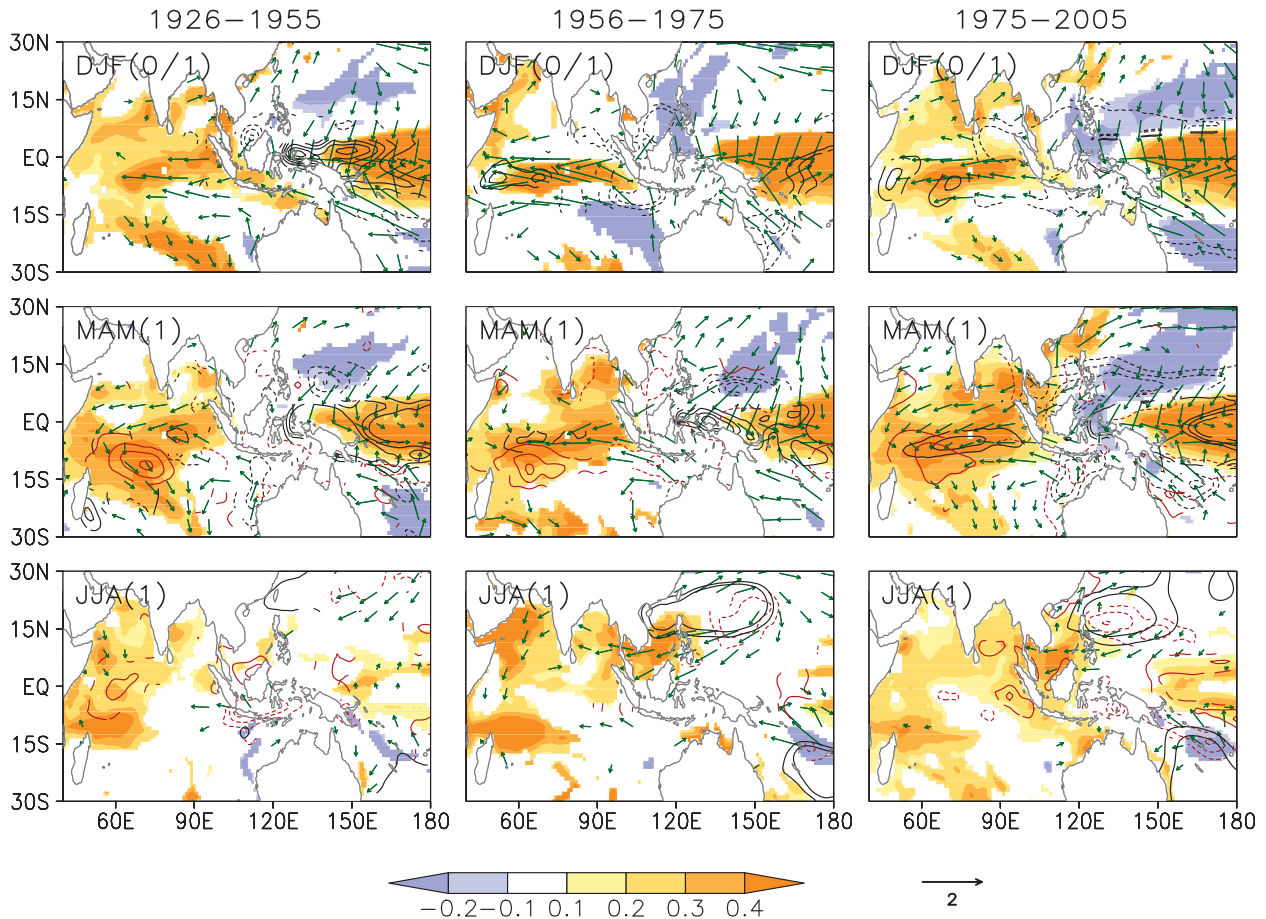


FIG. 19. Regressions of the NDJ (0–1) Niño-3.4 index with (top) DJF (0–1), (middle) MAM (1), and (bottom) JJA (1): SST (color shading, °C), surface wind (vectors, m s^{-1}), precipitation [black contours in DJF (0) and MAM (1), red contours in JJA (1), CI = 0.3 mm day^{-1} , starting from $\pm 0.3 \text{ mm day}^{-1}$], sea level height [red contours in MAM (1), CI = 2 cm, starting from $\pm 2 \text{ cm}$], and SLP [black contours in JJA (1), CI = 0.1 hPa , starting from $\pm 0.4 \text{ hPa}$]. Anomalies at an over 95% t -test confidence level for the periods (left)–(right) 1926–55, 1956–75, and 1976–2005 for GFDL-ESM2G.

et al. 2007). Accompanied with the NIO warming is an anomalous anticyclonic atmospheric circulation over NWP, together forming the robust climatic anomalies in summer following El Niño, consistent with previous studies (e.g., Xie et al. 2009; Huang et al. 2010). The formation of the NWP anticyclonic circulation and its relationship to NIO warming in CMIP5 models are investigated in a companion study (K. Hu et al. 2013, personal communication).

As in observations, the IOB mode and its correlation with ENSO display interdecadal variations in CMIP5 models. IOB variance responds to ENSO amplitude modulations in the Pacific. Specifically in summer following ENSO, the IOB mode and its capacitor effect on NWP climate strengthen when ENSO is vigorous and are insignificant when ENSO is weak.

The simulation of the IOB mode and key processes in CMIP5 models is good overall. Our analysis suggests that this may be due partly to the improvements in simulating

ENSO (Bellenger et al. 2013) and its teleconnections. This is encouraging, as ENSO is an important source of seasonal predictability. In the summer following ENSO specifically, the IOB mode and capacitor effect hold key to climate variability and predictability for the NWP and highly populated East Asia (Chowdary et al. 2010, 2011).

Acknowledgments. We wish to thank Y. Wu of LTO/SCSIO for help in downloading and processing CMIP5 data. We acknowledge the WCRP Working Group on Coupled Modelling, which is responsible for CMIP5, the climate modeling groups (listed in Table 1 of this paper) for producing and making available their model output, and we thank the U.S. Department of Energy's Program for Climate Model Diagnosis and Intercomparison (PCMDI) for providing coordinating support and organizing the analysis activity in partnership with the Global Organization for Earth System Science Portals. The satellite-merged SSH data, SODA reanalysis, and ERSST

were obtained from APDRC, University of Hawai'i at Mānoa (<http://apdrc.soest.hawaii.edu>), and HadISST and HadSST3 were obtained from the Met Office Hadley Centre (<http://www.metoffice.gov.uk>). This work is supported by MoST (2012CB955603, 2010CB950302), CAS (XDA05090404), NSFC (41176024, 41106010), LTO (LTOZZ1202), NSF, and JAMSTEC.

REFERENCES

- Alexander, M. A., I. Blade, M. Newman, J. R. Lanzante, N.-C. Lau, and J. D. Scott, 2002: The atmospheric bridge: The influence of ENSO teleconnections on air–sea interaction over the global oceans. *J. Climate*, **15**, 2205–2231.
- Allan, R., and T. Ansell, 2006: A new globally complete monthly historical gridded mean sea level pressure dataset (HadSLP2): 1850–2004. *J. Climate*, **19**, 5816–5842.
- An, S.-I., and B. Wang, 2000: Interdecadal change of the structure of the ENSO mode and its impact on the ENSO frequency. *J. Climate*, **13**, 2044–2055.
- , and F.-F. Jin, 2004: Nonlinearity and asymmetry of ENSO. *J. Climate*, **17**, 2399–2412.
- Annamalai, H., P. Liu, and S.-P. Xie, 2005: Southwest Indian Ocean SST variability: Its local effect and remote influence on Asian monsoons. *J. Climate*, **18**, 4150–4167.
- Bellenger, H., E. Guilyardi, J. Leloup, M. Lengaigne, and J. Vialard, 2013: ENSO representation in climate models: From CMIP3 to CMIP5. *Climate Dyn.*, doi:10.1007/s00382-013-1783-z, in press.
- Bunge, L., and A. J. Clarke, 2009: A verified estimation of the El Niño index Niño-3.4 since 1877. *J. Climate*, **22**, 3979–3992.
- Carton, J. A., and B. S. Giese, 2008: A reanalysis of ocean climate using Simple Ocean Data Assimilation (SODA). *Mon. Wea. Rev.*, **136**, 2999–3017.
- Chowdary, J. S., S.-P. Xie, J.-Y. Lee, Y. Kosaka, and B. Wang, 2010: Predictability of summer northwest Pacific climate in 11 coupled model hindcasts: Local and remote forcing. *J. Geophys. Res.*, **115**, D22121, doi:10.1029/2010JD014595.
- , —, J.-J. Luo, J. Hafner, S. Behera, Y. Masumoto, and T. Yamagata, 2011: Predictability of northwest Pacific climate during summer and the role of the tropical Indian Ocean. *Climate Dyn.*, **36**, 607–621, doi:10.1007/s00382-009-0686-5.
- , —, H. Tokinaga, Y. M. Okumura, H. Kubota, N. C. Johnson, and X.-T. Zheng, 2012: Interdecadal variations in ENSO teleconnection to the Indo-western Pacific for 1870–2007. *J. Climate*, **25**, 1722–1744.
- Collins, M., and Coauthors, 2010: The impact of global warming on the tropical Pacific Ocean and El Niño. *Nat. Geosci.*, **3**, 391–397.
- D'Arrigo, R., E. Cook, R. Wilson, R. Allan, and M. Mann, 2005: On the variability of ENSO over the past six centuries. *Geophys. Res. Lett.*, **32**, L03711, doi:10.1029/2004GL022055.
- Deser, C., A. S. Phillips, and M. A. Alexander, 2010: Twentieth century tropical sea surface temperature trends revisited. *Geophys. Res. Lett.*, **37**, L10701, doi:10.1029/2010GL043321.
- Du, Y., T. Qu, G. Meyers, Y. Masumoto, and H. Sasaki, 2005: Seasonal heat budget in the mixed layer of the southeastern tropical Indian Ocean in a high-resolution ocean general circulation model. *J. Geophys. Res.*, **110**, C04012, doi:10.1029/2004JC002845.
- , —, and —, 2008: Interannual variability of the sea surface temperature off Java and Sumatra in a global GCM. *J. Climate*, **21**, 2451–2465.
- , S.-P. Xie, K. Hu, and G. Huang, 2009: Role of air–sea interaction in the long persistence of El Niño–induced north Indian Ocean warming. *J. Climate*, **22**, 2023–2038.
- , L. Yang, and S.-P. Xie, 2011: Tropical Indian Ocean influence on northwest Pacific tropical cyclones in summer following strong El Niño. *J. Climate*, **24**, 315–322.
- Feng, M., C. Böning, A. Biastoch, E. Behrens, E. Weller, and Y. Masumoto, 2011: The reversal of the multi-decadal trends of the equatorial Pacific easterly winds, and the Indonesian Throughflow and Leeuwin Current transports. *Geophys. Res. Lett.*, **38**, L11604, doi:10.1029/2011GL047291.
- Fisher, R. A., 1921: On the “probable error” of a coefficient of correlation deduced from a small sample. *Metron*, **1**, 3–32.
- Gershunov, A., N. Schneider, and T. Barnett, 2001: Low frequency modulation of the ENSO–Indian monsoon rainfall relationship: Signal or noise? *J. Climate*, **14**, 2486–2492.
- Guilyardi, E., 2006: El Niño–mean state–seasonal cycle interactions in a multi-model ensemble. *Climate Dyn.*, **26**, 329–348.
- Hermes, J., and C. J. C. Reason, 2008: Annual cycle of the south Indian Ocean (Seychelles-Chagos) thermocline ridge in a regional ocean model. *J. Geophys. Res.*, **113**, C04035, doi:10.1029/2007JC004363.
- Huang, G., K. Hu, and S. P. Xie, 2010: Strengthening of tropical Indian Ocean teleconnection to the northwest Pacific since the mid-1970s: An atmospheric GCM study. *J. Climate*, **23**, 5294–5304.
- Izumo, T., C. de Boyer Montegut, J.-J. Luo, S. K. Behera, S. Masson, and T. Yamagata, 2008: The role of the western Arabian Sea upwelling in Indian monsoon rainfall variability. *J. Climate*, **21**, 5603–5623.
- , M. Lengaigne, J. Vialard, J.-J. Luo, T. Yamagata, and G. Madec, 2013: Influence of Indian Ocean Dipole and Pacific recharge on following year's El Niño: Interdecadal robustness. *Climate Dyn.*, doi:10.1007/s00382-012-1628-1, in press.
- Jing, Z., Y. Qi, and Y. Du, 2011: Upwelling in the continental shelf of northern South China Sea associated with 1997–1998 El Niño. *J. Geophys. Res.*, **116**, C02033, doi:10.1029/2010JC006598.
- Kanamitsu, M., W. Ebisuzaki, J. Woollen, S.-K. Yang, J. J. Hnilo, M. Fiorino, and G. L. Potter, 2002: NCEP–DOE AMIP-II Reanalysis (R-2). *Bull. Amer. Meteor. Soc.*, **83**, 1631–1643.
- Kawamura, R., T. Matsumura, and S. Iizuka, 2001: Role of equatorially asymmetric sea surface temperature anomalies in the Indian Ocean in the Asian summer monsoon and El Niño–Southern Oscillation coupling. *J. Geophys. Res.*, **106**, 4681–4693.
- Kennedy, J. J., N. A. Rayner, R. O. Smith, M. Saunby, and D. E. Parker, 2011: Reassessing biases and other uncertainties in sea surface temperature observations since 1850: 1. Measurement and sampling errors. *J. Geophys. Res.*, **116**, D14103, doi:10.1029/2010JD015218.
- Klein, S. A., B. J. Soden, and N.-C. Lau, 1999: Remote sea surface temperature variations during ENSO: Evidence for a tropical atmospheric bridge. *J. Climate*, **12**, 917–932.
- Kug, J.-S., S.-I. An, F.-F. Jin, and I.-S. Kang, 2005: Preconditions for El Niño and La Niña onsets and their relation to the Indian Ocean. *Geophys. Res. Lett.*, **32**, L05706, doi:10.1029/2004GL021674.
- Lau, N.-C., and M. J. Nath, 2003: Atmosphere–ocean variations in the Indo-Pacific sector during ENSO episodes. *J. Climate*, **16**, 3–20.
- Li, G., and B. Ren, 2012: Evidence for strengthening of the tropical Pacific Ocean surface wind speed during 1979–2001. *Theor. Appl. Climatol.*, **107**, 59–72.

- Li, J., S.-P. Xie, E. R. Cook, G. Huang, R. D'Arrigo, F. Liu, J. Ma, and X. Zheng, 2011: Interdecadal modulation of El Niño amplitude during the past millennium. *Nat. Climate Change*, **1**, 114–118, doi:10.1038/nclimate1086.
- Liu, Z., S. Vavrus, F. He, N. Wen, and Y. Zhong, 2005: Rethinking tropical ocean response to global warming: The enhanced equatorial warming. *J. Climate*, **18**, 4684–4700.
- Luo, J.-J., W. Sasakia, and Y. Masumoto, 2012: Indian Ocean warming modulates Pacific climate change. *Proc. Natl. Acad. Sci.*, **109**, 18 701–18 706.
- Masson, S., and Coauthors, 2005: Impact of barrier layer on winter-spring variability of the southeastern Arabian Sea. *Geophys. Res. Lett.*, **32**, L07703, doi:10.1029/2004GL021980.
- Masumoto, Y., and G. Meyers, 1998: Forced Rossby waves in the southern tropical Indian Ocean. *J. Geophys. Res.*, **103**, 27 589–27 602.
- Meehl, G. A., and Coauthors, 2007: Global climate projections. *Climate Change 2007: The Physical Science Basis*, S. Solomon et al., Eds., Cambridge University Press, 747–845.
- Merrifield, M. A., and M. E. Maltrud, 2011: Regional sea level trends due to a Pacific trade wind intensification. *Geophys. Res. Lett.*, **38**, L21605, doi:10.1029/2011GL049576.
- Montégut, C. B., J. Vialard, S. S. C. Shenoi, D. Shankar, F. Durand, C. Ethé, and G. Madec, 2007: Simulated seasonal and interannual variability of the mixed layer heat budget in the northern Indian Ocean. *J. Climate*, **20**, 3249–3268.
- Murtugudde, R., J. P. McCreary, and A. J. Busalacchi, 2000: Oceanic processes associated with anomalous events in the Indian Ocean with relevance to 1997–1998. *J. Geophys. Res.*, **105**, 3295–3306.
- Nicholls, N., 1984: The Southern Oscillation and Indonesian sea surface temperature. *Mon. Wea. Rev.*, **112**, 424–432.
- Ohba, M., and H. Ueda, 2005: Basin-wide warming in the equatorial Indian Ocean associated with El Niño. *SOLA*, **1**, 89–92.
- , and —, 2009: Role of nonlinear atmospheric response to SST on the asymmetric transition process of ENSO. *J. Climate*, **22**, 177–192.
- Okumura, Y. M., M. Ohba, C. Deser, and H. Ueda, 2011: A proposed mechanism for the asymmetric duration of El Niño and La Niña. *J. Climate*, **24**, 3822–3829.
- Perigaud, C., and P. Delecluse, 1993: Interannual sea level variations in the tropical Indian Ocean from Geosat and shallow-water simulations. *J. Phys. Oceanogr.*, **23**, 1916–1934.
- Power, S. B., and I. N. Smith, 2007: Weakening of the Walker circulation and apparent dominance of El Niño both reach record levels, but has ENSO really changed? *Geophys. Res. Lett.*, **34**, L18702, doi:10.1029/2007GL030854.
- Qu, T., and G. Meyers, 2005: Seasonal variation of barrier layer in the southeastern tropical Indian Ocean. *J. Geophys. Res.*, **110**, C11003, doi:10.1029/2004JC002816.
- Rayner, N. A., D. E. Parker, E. B. Horton, C. K. Folland, L. V. Alexander, D. P. Rowell, E. C. Kent, and A. Kaplan, 2003: Global analyses of sea surface temperature, sea ice, and night marine air temperature since the late nineteenth century. *J. Geophys. Res.*, **108**, 4407, doi:10.1029/2002JD002670.
- Saji, N. H., B. N. Goswami, P. N. Vinayachandran, and T. Yamagata, 1999: A dipole mode in the tropical Indian Ocean. *Nature*, **401**, 360–363.
- , S.-P. Xie, and T. Yamagata, 2006: Tropical Indian Ocean variability in the IPCC twentieth-century climate simulations. *J. Climate*, **19**, 4397–4417.
- Schott, F. A., S.-P. Xie, and J. P. McCreary Jr., 2009: Indian Ocean circulation and climate variability. *Rev. Geophys.*, **47**, RG1002, doi:10.1029/2007RG000245.
- Shinoda, T., M. A. Alexander, and H. H. Hendon, 2004: Remote response of the Indian Ocean to interannual SST variations in the tropical Pacific. *J. Climate*, **17**, 362–372.
- Smith, T. M., R. W. Reynolds, T. C. Peterson, and J. Lawrimore, 2008: Improvements to NOAA's historical merged land-ocean surface temperature analysis (1880–2006). *J. Climate*, **21**, 2283–2296.
- Taschetto, A. S., A. S. Gupta, H. H. Hendon, C. C. Ummerhofer, and M. H. England, 2011: The contribution of Indian Ocean sea surface temperature anomalies on Australian summer rainfall during El Niño events. *J. Climate*, **24**, 3734–3747.
- Taylor, K. E., R. J. Stouffer, and G. A. Meehl, 2012: An overview of CMIP5 and the experiment design. *Bull. Amer. Meteor. Soc.*, **93**, 485–498.
- Tokinaga, H., and Y. Tanimoto, 2004: Seasonal transition of SST anomalies in the tropical Indian Ocean during El Niño and Indian Ocean Dipole years. *J. Meteor. Soc. Japan*, **82**, 1007–1018.
- , S.-P. Xie, C. Deser, Y. Kosaka, and Y. M. Okumura, 2012: Slowdown of the Walker circulation driven by tropical Indo-Pacific warming. *Nature*, **491**, 439–443, doi:10.1038/nature11576.
- Urban, F. E., J. E. Cole, and J. T. Overpeck, 2000: Influence of mean climate change on climate variability from a 155-year tropical Pacific coral record. *Nature*, **407**, 989–993.
- Vecchi, G. A., and Coauthors, 2006: Weakening of tropical Pacific atmospheric circulation due to anthropogenic forcing. *Nature*, **441**, 73–76.
- Wallace, J. M., E. M. Rasmusson, T. P. Mitchell, V. E. Kousky, E. S. Sarachik, and H. von Storch, 1998: On the structure and evolution of ENSO-related climate variability in the tropical Pacific: Lessons from TOGA. *J. Geophys. Res.*, **103**, 14 241–14 259.
- Wang, B., R. Wu, and X. Fu, 2000: Pacific–East Asia teleconnection: How does ENSO affect East Asian climate? *J. Climate*, **13**, 1517–1536.
- , —, and T. Li, 2003: Atmosphere–warm ocean interaction and its impact on Asian–Australian monsoon variability. *J. Climate*, **16**, 1195–1211.
- Wang, C., and J. Picaut, 2004: Understanding ENSO physics—A review. *Earth's Climate: The Ocean–Atmosphere Interaction*, *Geophys. Monogr.*, Vol. 147, Amer. Geophys. Union, 21–48.
- Weare, B. C., 1979: A statistical study of the relationships between ocean surface temperatures and the Indian monsoon. *J. Atmos. Sci.*, **36**, 2279–2291.
- Wittenberg, A. T., 2009: Are historical records sufficient to constrain ENSO simulations? *Geophys. Res. Lett.*, **36**, L12702, doi:10.1029/2009GL038710.
- Wu, R., B. P. Kirtman, and V. Krishnamurthy, 2008: An asymmetric mode of tropical Indian Ocean rainfall variability in boreal spring. *J. Geophys. Res.*, **113**, D05104, doi:10.1029/2007JD009316.
- Wu, Y.-L., Y. Du, Y.-H. Zhang, and X.-T. Zheng, 2012: Interannual variability of sea surface temperature in the northern Indian Ocean associated with ENSO and IOD. *Atmos. Oceanic Sci. Lett.*, **5**, 295–300.
- Xie, P. P., and P. A. Arkin, 1997: Global precipitation: A 17-year monthly analysis based on gauge observations, satellite estimates, and numerical model outputs. *Bull. Amer. Meteor. Soc.*, **78**, 2539–2558.
- Xie, S.-P., and S. G. H. Philander, 1994: A coupled ocean–atmosphere model of relevance to the ITCZ in the eastern Pacific. *Tellus*, **46A**, 340–350.

- , H. Annamalai, F. Schott, and J. P. McCreary Jr., 2002: Origin and predictability of south Indian Ocean climate variability. *J. Climate*, **15**, 864–874.
- , Q. Xie, D. X. Wang, and W. T. Liu, 2003: Summer upwelling in the South China Sea and its role in regional climate variations. *J. Geophys. Res.*, **108**, 3261, doi:10.1029/2003JC001867.
- , K. Hu, J. Hafner, H. Tokinaga, Y. Du, G. Huang, and T. Sampe, 2009: Indian Ocean capacitor effect on Indo-western Pacific climate during the summer following El Niño. *J. Climate*, **22**, 730–747.
- , C. Deser, G. A. Vecchi, J. Ma, H. Teng, and A. T. Wittenberg, 2010: Global warming pattern formation: Sea surface temperature and rainfall. *J. Climate*, **23**, 966–986.
- Yamagata, T., S. K. Behera, J. J. Luo, S. Masson, M. R. Jury, and S. A. Rao, 2004: Coupled ocean-atmosphere variability in the tropical Indian Ocean. *Earth's Climate: The Ocean-Atmosphere Interaction, Geophys. Monogr.*, Vol. 147, Amer. Geophys. Union, 189–211.
- Yang, J., Q. Liu, S.-P. Xie, Z. Liu, and L. Wu, 2007: Impact of the Indian Ocean SST basin mode on the Asian summer monsoon. *Geophys. Res. Lett.*, **34**, L02708, doi:10.1029/2006GL028571.
- Yeh, S.-W., J. S. Kug, B. Dewitte, M. H. Kwon, B. P. Kirtman, and F. F. Jin, 2009: El Niño in a changing climate. *Nature*, **461**, 511–514, doi:10.1038/nature08316.
- Yokoi, T., T. Tozuka, and T. Yamagata, 2008: Seasonal variation of the Seychelles Dome. *J. Climate*, **21**, 3740–3754.
- , —, and —, 2009: Seasonal variation of the Seychelles Dome simulated in the CMIP3 models. *J. Phys. Oceanogr.*, **39**, 449–457.
- , —, and —, 2012: Seasonal and interannual variations of the SST above the Seychelles Dome. *J. Climate*, **25**, 800–814.
- Yu, L., and M. M. Rienecker, 1999: Mechanisms for the Indian Ocean warming during the 1997–98 El Niño. *Geophys. Res. Lett.*, **26**, 735–738.
- Yu, W., B. Xiang, L. Liu, and N. Liu, 2005: Understanding the origins of interannual thermocline variations in the tropical Indian Ocean. *Geophys. Res. Lett.*, **32**, L24706, doi:10.1029/2005GL024327.
- Zheng, X.-T., S.-P. Xie, G. A. Vecchi, Q. Liu, and J. Hafner, 2010: Indian Ocean dipole response to global warming: Analysis of ocean-atmospheric feedbacks in a coupled model. *J. Climate*, **23**, 1240–1253.
- , —, and Q. Liu, 2011: Response of the Indian Ocean Basin mode and its capacitor effect to global warming. *J. Climate*, **24**, 6146–6164.
- , —, Y. Du, L. Liu, G. Huang, and Q. Liu, 2013: Indian Ocean Dipole response to global warming in the CMIP5 multimodel ensemble. *J. Climate*, **26**, 6067–6080.